2009-01-01

Delayed-Detached-Eddy Simulation of Shock Wave/Turbulent Boundary Layer Interaction

Patricia X. Coronado Domenge
University of Miami, patatas514@gmail.com

UNIVERSITY OF MIAMI

DELAYED-DETACHED-EDDY SIMULATION OF SHOCK WAVE/TURBULENT BOUNDARY LAYER INTERACTION

By

Patricia X. Coronado Domenge

A THESIS

Submitted to the Faculty
of the University of Miami
in partial fulfillment of the requirements for
the degree of Master of Science

Coral Gables, Florida

August 2009

UNIVERSITY OF MIAMI

A thesis submitted in partial fulfillment of
the requirements for the degree of
Master of Science

DELAYED-DETACHED-EDDY SIMULATION OF SHOCK WAVE/TURBULENT BOUNDARY LAYER INTERACTION

Patricia X. Coronado Domenge

Approved:

Gecheng Zha, Ph.D.
Associate Professor of
Mechanical & Aerospace Engineering

Terri A. Scandura, Ph.D.
Dean of the Graduate School

Jizhou Song, Ph.D.
Assistant Professor of
Mechanical & Aerospace Engineering

Manuel A. Huerta, Ph.D.
Professor of
Department of Physics

Na Li, Ph.D.
Assistant Professor of
Mechanical & Aerospace Engineering

CORONADO DOMENGE, PATRICIA X. (M.S., Mechanical Engineering)
Delayed-Detached-Eddy Simulation of (August 2009)
Shock Wave/Turbulent Boundary Layer Interaction

Abstract of a thesis at the University of Miami.

Thesis supervised by Professor Gecheng Zha.
No. of pages in text. (51)

The purpose of this thesis is to study the shock/wave turbulent boundary layer interaction by using delayed-detached-eddy simulation (DDES) model with a low diffusion E-CUSP (LDE) scheme with fifth-order WENO scheme. The results show that DDES simulation provides improved results for the shock wave/turbulent boundary layer interaction compared to those of its predecessor the detached-eddy simulation (DES). The computation of mesh refinement indicates that the grid density has significant effects on the results of DES, while being resolved by applying DDES simulation.

Spalart in 1997 developed the Detached-Eddy Simulation (DES) model, which is a hybrid RANS and LES method, to overcome the intensive CPU requirement from LES models. Near the solid surface within a wall boundary layer, the unsteady RANS model is realized. Away from the wall surface, the model automatically converts to LES.

The Delayed-Detached-Eddy Simulation (DDES) was suggested by Spalart in 2006 to improve the DES model previously developed. The transition from the RANS model to LES in DES is not grid spacing independent, therefore a blending function is introduced to the recently developed DDES model to make the transition from RANS to LES grid spacing independent. The DDES is validated by computing a 3D subsonic flat plate turbulent boundary layer.

The first case studied using DDES is a 3D transonic channel with shock/turbulent boundary layer interaction. It consists of two straight side walls, a straight top wall, and a varying shape in span-wise direction for a bottom wall. The second case studied consists of a 3D transonic inlet-diffuser. Both results are compared with experimental data. The computed results of the transonic channel agree well with experimental data.

Acknowledgment

I would like to express my deepest gratitude to my academic advisor Professor Gecheng Zha for this opportunity as well as for his guidance in my study and research.

I would also like to thank Dr. Baoyuan Wang for implementing the delayed detached eddy simulation and my colleague Hongsik IM for his constant help and instruction. Whenever I asked he was there to help.

This research would definitely not have been possible without the help and constant support of my friends and family. Special thanks go to tuma, tupa, and my best friend Maygen. Even when things seemed a little dark, they would never let me give up. Without them this would never have been finished.

Contents

List of Figures

List of Tables

Chapter 1

Introduction

In order to resolve the aerodynamic non-linearity of shock wave/tubulent boundary layer interaction and flow separation, it is critical to employ advanced turbulence modeling. The methods based on Reynolds Average Navier-Strokes (RANS) equations are widely used for the simulation of turbulent flows, although they are not able to simulate the flow separation in an accurate manner. RANS methods calculate the large scale eddies using a universal model. Such universal model does not exist for the large scale turbulence that is affected by flow geometry and boundary conditions.

Large Eddy Simulation (LES) is promising, performing better than the RANS model, while overcoming its disadvantages. In LES, the governing equations are spatially filtered on the scale of the numerical grid. This resolves the unsteady large scale turbulent structures, while modeling the small scale high frequency structures of turbulence. The small scale eddies, which are generally more homogeneous and universal, are modeled, and the large energy containing scales are directly simulated. The large eddies are strongly affected by the flow field geometry boundaries, making the direct computation of the large eddies by LES more accurate than the modeling of the large eddies by RANS. The effect of the unresolved small scales of motion is modeled by a sub-grid-scale (SGS) model [3–7] or by the inherent dissipation in the numerical schemes [8–14]. Given that the statistics of the

small scale turbulence are more isotropic and universal, a general physical model for small scale eddies is more plausible.

1.1 Detached-Eddy-Simulation

For high Reynolds number flows such as those of turbo-machinery blades and transonic wings, to resolve the wall boundary layer, LES needs the CPU resource not much less than the Direct Numerical Simulation(DNS). This makes the LES too expensive for high Reynolds number flow calculations and therefore it is not hopeful for LES to be rigorously implemented for another 4 decades in engineering applications [15]. Spalart et al. developed the so called detached-eddy simulation (DES) strategy [15], which is a hybrid RANS and LES method, to overcome the intensive CPU requirement for LES. Near the solid surface within the wall boundary layer, the unsteady RANS model is realized. Away from the wall surface, the model automatically converts to LES. By using the RANS model near the wall, the fine mesh resolution of LES to resolve the viscous sublayer is avoided and the CPU time can be tremendously reduced. The motivation of DES is that the LES is powerful in regions of massive separation and other free shear flows such as jets, but is much too costly in the large area of thin wall boundary layers.

In 2001, Spalart gave a grid guidance for DES [16, 17], which divides a flow domain with solid walls to Euler region, LES region, and RANS region. The LES region is composed of Viscous, Focus and Departure region. In the RANS region, the domain is further divided to Viscous region and Outer region. Spalart's DES grid guidance gives sufficient grid resolution for LES region and the transition to Euler region from RANS region. The grid size is dramatically reduced compared to the pure LES.

Even though the DES concept is much newer than RANS and LES concept, its application for turbulence simulation has already achieved encouraging success as shown in the work of Wang [18] [19] and Tarvin et al. (1999) [20], Spalart (2001) [16, 17], Forsythe et

al.(2002) [21], Viswanathan et al. [22], Squires et al. [23, 24], Hsnsen, et al. (2003) [25], Subbareddy et al. (2005) [26]. These flows calculated using DES include those for airfoils, cylinders, forbodies, base flows, etc. The results are qualitatively and quantitatively better than the solutions using RANS. DES appears to be a suitable compromise between the physical models of turbulence and CPU efficiency. In those DES applications, almost all the algorithms use 2nd order accuracy except that of Tarvin et al. (1999) [20], which employs fifth order upwind scheme for the inviscid convective terms in space.

1.2 Delayed-Detached-Eddy Simulation

After the successful DES application was first proposed in 1997, a defect of the first generation DES model(DES97) [15] has been also exposed, being that the transition from the RANS model to LES in DES97 may not be grid spacing independent [27]. DES was originally designed to treat the entire boundary layer using a RANS model and to use LES for separated flow regions. A fine mesh with grid spacing much smaller than the boundary layer thickness may exhibit an incorrect behavior in boundary layers and shallow separation regions due to locating the RANS/LES transition within the boundary layer. The grid spacing could be fine enough for the DES length scale to follow the LES branch, which will lower the eddy viscosity below the RANS level. The resolved Reynolds stresses determined from the velocity fluctuation (LES content) may be lacking because the resolution is not fine enough to fully support it. The DES limiter then reduces the eddy viscosity, and therefore the modeled Reynolds stresses. This phenomenon is referred as modeled-stress depletion (MSD) [27]. This drawback is also considered as one of the possible causes for the inaccurate prediction of flow separation region size with suction flow control when the DES is used as indicated by Rumsey [28].

To overcome the MSD problem and make the DES limiter independent of grid spacing, Spalart suggested a modification to the original DES97 model in 2006 [27], referred to as

Delayed-Detached-Eddy Simulation (DDES). A blending function similar to the one used by Menter and Kuntz [29] for the SST model is introduced to limit the DES length scale to ensure the transition of RANS to LES be independent of grid spacing. The DDES model has demonstrated excellent agreement with experiment and a significant improvement over the DES97 for the tested cases, which include a flat plat boundary layer resolved with mesh spacing significantly smaller than the boundary layer thickness, a circular cylinder, a single airfoil with weak separation near trailing edge, the backward facing step with large separation region, and a multi-element airfoil. The predicted separation onset and separation region length agree well with the experiments.

In this thesis, the DDES of Spalart [27] based on the Spalart-Allmaras one equation turbulence model will be employed with the recently developed low diffusion E-CUSP scheme [1] with fifth-order WENO scheme [30, 31] for the inviscid fluxes, in order to investigate the shock wave/turbulet boundary layer interaction. The first case studied is a 3D Transonic Channel and the second case is a 3D Transonic Inlet-Diffuser.

Chapter 2

Governing Equations

The governing equations for the flow field computation are the spatially filtered 3D general Navier-Stokes equations in generalized coordinates and can be expressed as follows:

$$\frac{\partial \mathbf{Q}'}{\partial t} + \frac{\partial \mathbf{E}'}{\partial \xi} + \frac{\partial \mathbf{F}'}{\partial \eta} + \frac{\partial \mathbf{G}'}{\partial \zeta} = \frac{1}{\mathrm{Re}} \left(\frac{\partial \mathbf{E}'_{\mathbf{v}}}{\partial \xi} + \frac{\partial \mathbf{F}'_{\mathbf{v}}}{\partial \eta} + \frac{\partial \mathbf{G}'_{\mathbf{v}}}{\partial \zeta} \right) \tag{2.1}$$

where Re is the Reynolds number defined as

$$Re = \frac{\rho_\infty L u_\infty}{\mu_\infty} \tag{2.2}$$

and

$$\mathbf{Q}' = \frac{\mathbf{Q}}{J} \tag{2.3}$$

$$\mathbf{E}' = \frac{1}{J}(\xi_t \mathbf{Q} + \xi_x \mathbf{E} + \xi_y \mathbf{F} + \xi_z \mathbf{G}) \tag{2.4}$$

$$\mathbf{F}' = \frac{1}{J}(\eta_t \mathbf{Q} + \eta_x \mathbf{E} + \eta_y \mathbf{F} + \eta_z \mathbf{G}) \tag{2.5}$$

$$\mathbf{G}' = \frac{1}{J}(\zeta_t \mathbf{Q} + \zeta_x \mathbf{E} + \zeta_y \mathbf{F} + \zeta_z \mathbf{G}) \tag{2.6}$$

$$\mathbf{E}'_{\mathbf{v}} = \frac{1}{J}(\xi_x \mathbf{E}_{\mathbf{v}} + \xi_y \mathbf{F}_{\mathbf{v}} + \xi_z \mathbf{G}_{\mathbf{v}}) \tag{2.7}$$

$$\mathbf{F}'_{\mathbf{v}} = \frac{1}{J}(\eta_x \mathbf{E}_{\mathbf{v}} + \eta_y \mathbf{F}_{\mathbf{v}} + \eta_z \mathbf{G}_{\mathbf{v}}) \tag{2.8}$$

$$\mathbf{G}'_{\mathbf{v}} = \frac{1}{J}(\zeta_x \mathbf{E}_{\mathbf{v}} + \zeta_y \mathbf{F}_{\mathbf{v}} + \zeta_z \mathbf{G}_{\mathbf{v}}) \tag{2.9}$$

where J is the transformation Jacobian. The Navier-Stokes equations noted in Eq.(2.1) are normalized to bring the numerical round-off error to its minimum, the normalization procedure is found in [32].

The conservative variable vector $\mathbf{Q}$, the inviscid flux vectors $\mathbf{E}$, $\mathbf{F}$, and $\mathbf{G}$ are given as the following.

$$\mathbf{Q} = \begin{pmatrix} \bar{\rho} \\ \bar{\rho}\tilde{u} \\ \bar{\rho}\tilde{v} \\ \bar{\rho}\tilde{w} \\ \bar{\rho}\tilde{e} \end{pmatrix}, \mathbf{E} = \begin{pmatrix} \bar{\rho}\tilde{u} \\ \bar{\rho}\tilde{u}^2 + \bar{p} \\ \bar{\rho}\tilde{u}\tilde{v} \\ \bar{\rho}\tilde{u}\tilde{w} \\ (\bar{\rho}\tilde{e} + \bar{p})\tilde{u} \end{pmatrix}, \mathbf{F} = \begin{pmatrix} \bar{\rho}\tilde{v} \\ \bar{\rho}\tilde{v}\tilde{u} \\ \bar{\rho}\tilde{v}^2 + \bar{p} \\ \bar{\rho}\tilde{v}\tilde{w} \\ (\bar{\rho}\tilde{e} + \bar{p})\tilde{v} \end{pmatrix}, \mathbf{G} = \begin{pmatrix} \bar{\rho}\tilde{w} \\ \bar{\rho}\tilde{w}\tilde{u} \\ \bar{\rho}\tilde{w}\tilde{v} \\ \bar{\rho}\tilde{w}^2 + \bar{p} \\ (\bar{\rho}\tilde{e} + \bar{p})\tilde{w} \end{pmatrix}$$

The inviscid fluxes in generalized coordinate system are expressed as:

$$\mathbf{E}' = \begin{bmatrix} \bar{\rho}U \\ \bar{\rho}\tilde{u}U + l_x\bar{p} \\ \bar{\rho}\tilde{v}U + l_y\bar{p} \\ \bar{\rho}\tilde{w}U + l_z\bar{p} \\ (\bar{\rho}\tilde{e} + \bar{p})U - l_t\bar{p} \end{bmatrix}, \mathbf{F}' = \begin{bmatrix} \bar{\rho}V \\ \bar{\rho}\tilde{u}V + m_x\bar{p} \\ \bar{\rho}\tilde{v}V + m_y\bar{p} \\ \bar{\rho}\tilde{w}V + m_z\bar{p} \\ (\bar{\rho}\tilde{e} + \bar{p})V - m_t\bar{p} \end{bmatrix}, \mathbf{G}' = \begin{bmatrix} \bar{\rho}W \\ \bar{\rho}\tilde{u}W + n_x\bar{p} \\ \bar{\rho}\tilde{v}W + n_y\bar{p} \\ \bar{\rho}\tilde{w}W + n_z\bar{p} \\ (\bar{\rho}\tilde{e} + \bar{p})W - n_t\bar{p} \end{bmatrix}$$

where U, V and W are the contravariant velocities in ξ, η and ζ directions.

$$
\begin{aligned}
U &= l_t + \mathbf{l} \bullet \mathbf{V} = l_t + l_x\tilde{u} + l_y\tilde{v} + l_z\tilde{w} \\
V &= m_t + \mathbf{m} \bullet \mathbf{V} = m_t + m_x\tilde{u} + m_y\tilde{v} + m_z\tilde{w} \\
W &= n_t + \mathbf{n} \bullet \mathbf{V} = n_t + n_x\tilde{u} + n_y\tilde{v} + n_z\tilde{w}
\end{aligned} \tag{2.10}
$$

$\mathbf{l}, \mathbf{m}, \mathbf{n}$ are the normal vectors on ξ, η, ζ surfaces with their magnitudes equal to the elemental surface area and pointing to the directions of increasing ξ, η, ζ.

$$
\mathbf{l} = \frac{\nabla\xi}{J},\ \mathbf{m} = \frac{\nabla\eta}{J},\ \mathbf{n} = \frac{\nabla\zeta}{J} \tag{2.11}
$$

$$
l_t = \frac{\xi_t}{J},\ m_t = \frac{\eta_t}{J},\ n_t = \frac{\zeta_t}{J} \tag{2.12}
$$

$$
\mathbf{E_v} = \begin{pmatrix} 0 \\ \bar{\tau}_{xx} + \sigma_{xx} \\ \bar{\tau}_{xy} + \sigma_{xy} \\ \bar{\tau}_{xz} + \sigma_{xz} \\ Q_x \end{pmatrix}, \mathbf{F_v} = \begin{pmatrix} 0 \\ \bar{\tau}_{yx} + \sigma_{yx} \\ \bar{\tau}_{yy} + \sigma_{yy} \\ \bar{\tau}_{yz} + \sigma_{yz} \\ Q_y \end{pmatrix}, \mathbf{G_v} = \begin{pmatrix} 0 \\ \bar{\tau}_{zx} + \sigma_{zx} \\ \bar{\tau}_{zy} + \sigma_{zy} \\ \bar{\tau}_{zz} + \sigma_{zz} \\ Q_z \end{pmatrix},
$$

In the above equations, ρ is the density, u, v, w are the Cartesian velocity components in x, y, z directions, p is the static pressure, and e is the total energy per unit mass. The overbar denotes a regular filtered variable, and the tilde is used to denote the Favre filtered variable. The $\bar{\tau}$ is the molecular viscous stress tensor and is estimated as:

$$
\bar{\tau}_{ij} = \frac{2}{3}\tilde{\mu}\frac{\partial\tilde{u}_k}{\partial x}_k \delta_{ij} + \mu(\frac{\partial\tilde{u}_i}{\partial x_j} + \frac{\partial\tilde{u}_j}{\partial x_i}), \qquad i, j = 1, 2, 3 \tag{2.13}
$$

The above equation is in the tensor form, where the subscript 1, 2, 3 represent the coordinates, x, y, z and the Einstein summation convention is used.

The molecular viscosity $\tilde{\mu} = \tilde{\mu}(\tilde{T})$ is determined by Sutherland law.

The σ is the subgrid scale stress tensor due to the filtering process and is expressed as:

$$\sigma_{ij} = -\bar{\rho}(\widetilde{u_i u_j} - \tilde{u}_i \tilde{u}_j) \tag{2.14}$$

The energy flux Q is expressed as:

$$Q_i = \tilde{u}_j(\bar{\tau}_{ij} + \sigma_{ij}) - \bar{q}_i + \Phi_i \tag{2.15}$$

where Φ is the subscale heat flux:

$$\Phi_i = -C_p \bar{\rho}(\widetilde{u_i T} - \tilde{u}_i \tilde{T}) \tag{2.16}$$

The $\bar{q}_i$ is the molecular heat flux:

$$\bar{q}_i = -\frac{C_p \tilde{\mu}}{Pr} \frac{\partial \tilde{T}}{\partial x_i} \tag{2.17}$$

$$\bar{\rho}\tilde{e} = \frac{\bar{p}}{(\gamma - 1)} + \frac{1}{2}\bar{\rho}(\tilde{u}^2 + \tilde{v}^2 + \tilde{w}^2) + \rho k \tag{2.18}$$

where γ is the ratio of specific heats, ρk is the subscale kinetic energy per unit volume.

$$\rho k = \frac{1}{2}\bar{\rho}(\widetilde{u_i u_i} - \tilde{u}_i \tilde{u}_i) = -\frac{1}{2}\sigma_{ii} \tag{2.19}$$

In the current simulations, the ρk in Eq.(2.18) is omitted based on the assumption that the effect is small.

2.1 Detached-Eddy-Simulation

DES is a hybrid method which involves both the RANS model and the LES model. This is done by applying the RANS model near the wall, and the LES model everywhere else

away from the wall. The Navier-Stokes equations can then be solved using the DES model suggested by Spalart et al. [15] as the following.

First the sub-grid scale stresses are determined as:

$$\sigma_{ij} = \mu_{DES}(\frac{\partial \tilde{u}_i}{\partial x_j} + \frac{\partial \tilde{u}_j}{\partial x_i} - \frac{2}{3}\frac{\partial \tilde{u}_k}{\partial x}_k \delta_{ij}) - \frac{2}{3}\rho k \delta_{ij} \qquad i,j = 1,2,3 \tag{2.20}$$

The turbulent heat flux will be evaluated by:

$$\Phi_i = C_p \frac{\mu_{DES}}{Pr_t}\frac{\partial \tilde{T}}{\partial x_i} \tag{2.21}$$

where

$$\mu_{DES} = \rho \nu_t = \rho \tilde{\nu} f_{v1} \tag{2.22}$$

$\tilde{\nu}$ is a working variable and is determined by the following Spalart-Allmaras model [15, 22, 33, 34]:

$$\frac{D\tilde{\nu}}{Dt} = c_{b1}\tilde{S}\tilde{\nu}\,(1-f_{t2}) - [c_{w1}f_w - \frac{c_{b1}}{k^2}f_{t2}][\frac{\tilde{\nu}}{d}]^2 + \frac{1}{\sigma}[\nabla\cdot((\nu+\tilde{\nu})\nabla\tilde{\nu}) + c_{b2}(\nabla\tilde{\nu})^2] + f_{t1}\,(\Delta q)^2 \tag{2.23}$$

In generalized coordinate system, the conservative form of Eq.(2.23) is given as the following:

$$\frac{\partial \frac{1}{J}\rho\tilde{\nu}}{\partial t} + \frac{\partial \rho\tilde{\nu}U}{\partial \xi} + \frac{\partial \rho\tilde{\nu}V}{\partial \eta} + \frac{\partial \rho\tilde{\nu}W}{\partial \zeta} = \frac{1}{Re}\left(\frac{\partial \frac{\rho}{\sigma}(\nu+\tilde{\nu})\,(\mathbf{l}\bullet\nabla\tilde{\nu})}{\partial \xi}\right.$$
$$\left. .+\frac{\partial \frac{\rho}{\sigma}(\nu+\tilde{\nu})\,(\mathbf{m}\bullet\nabla\tilde{\nu})}{\partial \eta} + \frac{\partial \frac{\rho}{\sigma}(\nu+\tilde{\nu})\,(\mathbf{n}\bullet\nabla\tilde{\nu})}{\partial \zeta} + \frac{1}{J}S_\nu\right) \tag{2.24}$$

where

$$S_\nu = \rho C_{b1}(1-f_{t2})\tilde{S}\tilde{\nu} + \frac{1}{Re}\left[-\rho\left(C_{w1}f_w - \frac{C_{b1}}{\kappa^2}f_{t2}\right)\left(\frac{\tilde{\nu}}{d}\right)^2 + \frac{\rho}{\sigma}C_{b2}(\nabla\tilde{\nu})^2 - \frac{1}{\sigma}(\nu+\tilde{\nu})\nabla\tilde{\nu}\bullet\nabla\rho\right] + Re\left[\rho f_{t1}(\Delta q)^2\right] \tag{2.25}$$

Eq.(2.24) is then coupled with Eq.(2.1) when it is solved.

The eddy viscosity ν_t is obtained from:

$$\nu_t = \tilde{\nu} f_{v1} \qquad f_{v1} = \frac{\chi^3}{\chi^3 + c_{v1}^3} \qquad \chi = \frac{\tilde{\nu}}{\nu} \tag{2.26}$$

where ν is the molecular viscosity. The resulting term is:

$$\tilde{S} = S + \frac{\tilde{\nu}}{k^2 d^2} f_{v2}, \qquad f_{v2} = 1 - \frac{\chi}{1+\chi f_{v1}} \tag{2.27}$$

where S is the magnitude of the vorticity. The function f_w is given by

$$f_w = g\left(\frac{1+c_{w3}^6}{g^6+c_{w3}^6}\right)^{1/6}, \qquad g = r + c_{w2}(r^6 - r), \qquad r = \frac{\tilde{\nu}}{\tilde{S}k^2d^2} \tag{2.28}$$

The function f_{t2} is given by

$$f_{t2} = C_{t3} exp\left(-C_{t4}\chi^2\right) \tag{2.29}$$

and the trip function f_{t1} is

$$f_{t1} = C_{t1} g_t exp\left[-C_{t2}\frac{\omega_t^2}{\Delta U^2}\left(d^2 + g_t^2 d_t^2\right)\right], \; g_t = min\left(0.1, \frac{\Delta q}{\omega_t \Delta x_t}\right) \tag{2.30}$$

where, ω_t is the wall vorticity at the wall boundary layer trip location, d is the distance to the closest wall, d_t is the distance of the field point to the trip location, Δq is the difference of the velocities between the field point and the trip location, and Δx_t is the grid spacing along the wall at the trip location.

The values of the coefficients are given as:

$$C_{b1} = 0.1355,\ C_{b2} = 0.622,\ \sigma = \frac{2}{3},$$
$$C_{w1} = \frac{c_{b1}}{k^2} + (1 + c_{b2})/\sigma,\ C_{w2} = 0.3,\ C_{w3} = 2.0,$$
$$\kappa = 0.41,\ C_{v1} = 7.1,\ C_{t1} = 1.0,\ C_{t2} = 2.0,\ C_{t3} = 1.1,\ C_{t4} = 2.0$$

In DES, c_{t1} and c_{t3} are set as zero. The distance to the nearest wall, d, is replaced by $\tilde{d}$ as

$$\tilde{d} = min(d, C_{DES}\Delta) \tag{2.31}$$

where Δ is the largest spacing of the grid cell in all the directions.

Within the boundary layer close to walls, $\tilde{d} = d$, hence the turbulence is simulated by the RANS mode determined by the Spalart-Allmaras model [33]. Away from the boundary layer, $\tilde{d} = C_{DES}\Delta$ is most of the cases. When the production and destruction terms of the model are balanced, the length scale $\tilde{d}$ will have a Smagorinsky-like eddy viscosity and the turbulence is simulated by the LES model. Analogous to the classical LES theory, the length scale Δ is to cascade the energy to the grid size. The coefficient $C_{DES} = 0.65$ is used as set in the homogeneous turbulence [35]. The Pr_t may take the value of 0.9 within the boundary layer for RANS mode and 0.5 for LES mode away from the wall surface. Eq.(2.23) will be extended to generalized coordinates and will be coupled and solved together with the filtered Navier-Stokes equations, Eq.(2.1).

2.2 Delayed-Detached-Eddy Simulation

The DDES formulation introduced by Sparlat et al. [27] suggests some modifications to his previous DES model [15] , given that in wide boundary layers and shallow separation regions the DES simulation can present an erroneous behavior. This may occur when the thickness of the boundary layer is greater than the grid spacing parallel to the wall, making the transition from RANS to LES earlier. With the new modified DDES, the RANS model is retained longer for thick boundary layers independent of the grid spacing. The DES

model is adjusted as follows.

The parameter r is modified from the S-A definition to:

$$r_d = \frac{\nu_t + \nu}{(U_{i,j}U_{i,j})^{0.5}k^2d^2} \tag{2.32}$$

where $U_{i,j}$ are the velocity gradients, and the subscript d refers to delayed for DDES. This parameter is modified in this form so it can be applied to any eddy-viscous model.

r_d is applied in the following function

$$f_d = 1 - tanh([8r_d]^3) \tag{2.33}$$

The coefficients 8 and 3 are acquired from DDES flat plate boundary layer tests [27] by matching the solution to the RANS values. In this way the DES $\tilde{d}$ can be modified and be definied for DDES as follows:

$$\tilde{d} = d - f_d max(0, d - C_{DES}\Delta) \tag{2.34}$$

This modification in $\tilde{d}$ reduces the grey transition area between RANS and LES. The qualitative change of the new $\tilde{d}$ is very significant, depending now on the eddy-viscosity field. The DDES model now can refuse the transition to LES if not ready, when the function f_d, using the value of r_d, indicates that the point still lies within the boundary layer. The opposite also occurs, when there is massive separation indicated by f_d, the change from RANS to LES takes place in the simulation.

Chapter 3

The Numerical Method

The DDES of Spalart [27] based on the Spalart-Allmaras one equation turbulence model is to be employed with the recently developed low diffusion E-CUSP scheme [1] with fifth-order WENO scheme for the inviscid fluxes and 4th order central differencing scheme for viscous terms [30, 31]. These schemes that use finite difference methods to discretize the governing equations are introduced in this chapter.

3.1 The Low Diffusion E-CUSP (LDE) Scheme [1]

The idea behind the LDE scheme is to split the inviscid flux into the convective flux E^c and the pressure flux E^p. With the one extra equation from the S-A model for DES and DDES, the splitting is basically the same as the original scheme for the Euler equation and is straightforward [36]. This is an advantage over the Roe scheme [37], for which the eigenvectors need to be derived when any extra equation is added to the governing equations. In [38], the LDE scheme is shown to be more efficient than the Roe scheme when the S-A one equation turbulence model is coupled.

In generalized coordinate system, the flux **E** can be split as follows:

$$\mathbf{E}' = E^c + E^p = \begin{pmatrix} \rho U \\ \rho u U \\ \rho v U \\ \rho w U \\ \rho e U \\ \rho \tilde{\nu} U \end{pmatrix} + \begin{pmatrix} 0 \\ l_x p \\ l_y p \\ l_z p \\ p\overline{U} \\ 0 \end{pmatrix} \tag{3.1}$$

where, U is the contravariant velocity in ξ direction and is defined as the following:

$$U = l_t + l_x u + l_y v + l_z w \tag{3.2}$$

$\overline{U}$ is defined as:

$$\overline{U} = l_x u + l_y v + l_z w \tag{3.3}$$

The convective term, E^c is evaluated by Edward's H-CUSP LDFSS scheme [39,40] by,

$$E^c = \rho U \begin{pmatrix} 1 \\ u \\ v \\ w \\ e \\ \tilde{\nu} \end{pmatrix} = \rho U f^c,\ f^c = \begin{pmatrix} 1 \\ u \\ v \\ w \\ e \\ \tilde{\nu} \end{pmatrix} \tag{3.4}$$

let

$$C = c\left(l_x^2 + l_y^2 + l_z^2\right)^{\frac{1}{2}} \tag{3.5}$$

where $c = \sqrt{\gamma RT}$ is the speed of sound. Then the convective flux at interface $i + \frac{1}{2}$ is calculated as:

$$E^c_{i+\frac{1}{2}} = C_{\frac{1}{2}}\left[\rho_L C^+ f^c_L + \rho_R C^- f^c_R\right] \tag{3.6}$$

where, the subscripts L and R represent the left and right hand sides of the interface. The Mach number splitting of Edwards [39, 40] is borrowed to determine c^+ and c^- as the following:

$$\begin{aligned}
&C_{\frac{1}{2}} = \tfrac{1}{2}\left(C_L + C_R\right),\ C^+ = \alpha^+_L\left(1+\beta_L\right)M_L - \beta_L M^+_L - M^+_{\frac{1}{2}}\\
&C^- = \alpha^-_R\left(1+\beta_R\right)M_R - \beta_R M^-_R + M^-_{\frac{1}{2}}\\
&M_L = \tfrac{U_L}{C_{\frac{1}{2}}},\ M_R = \tfrac{U_R}{C_{\frac{1}{2}}}\\
&\alpha_{L,R} = \tfrac{1}{2}\left[1 \pm sign\left(M_{L,R}\right)\right]\\
&\beta_{L,R} = -max\left[0, 1 - int\left(\left|M_{L,R}\right|\right)\right]\\
&M^+_{\frac{1}{2}} = M_{\frac{1}{2}}\tfrac{C_R + C_L\Phi}{C_R + C_L},\ M^-_{\frac{1}{2}} = M_{\frac{1}{2}}\tfrac{C_L + C_R\Phi^{-1}}{C_R + C_L},\ \Phi = \tfrac{\left(\rho C^2\right)_R}{\left(\rho C^2\right)_L}\\
&M_{\frac{1}{2}} = \beta_L\delta^+ M^-_L - \beta_R\delta^- M^+_R\\
&M^\pm_{L,R} = \pm\tfrac{1}{4}\left(M_{L,R} \pm 1\right)^2\\
&\delta^\pm = \tfrac{1}{2}\left\{1 \pm sign\left[\tfrac{1}{2}\left(M_L + M_R\right)\right]\right\}
\end{aligned}$$

The pressure flux, E^p is evaluated as the following

$$E^p_{i+\frac{1}{2}} = \begin{pmatrix} 0 \\ \mathscr{P}^+ p\, l_x \\ \mathscr{P}^+ p\, l_y \\ \mathscr{P}^+ p\, l_z \\ \frac{1}{2}p\left[\overline{U} + \overline{C}_{\frac{1}{2}}\right] \\ 0 \end{pmatrix}_L + \begin{pmatrix} 0 \\ \mathscr{P}^- p\, l_x \\ \mathscr{P}^- p\, l_y \\ \mathscr{P}^- p\, l_z \\ \frac{1}{2}p\left[\overline{U} - \overline{C}_{\frac{1}{2}}\right] \\ 0 \end{pmatrix}_R \tag{3.7}$$

The contravariant speed of sound $\overline{C}$ in the pressure vector is consistent with $\overline{U}$. It is

computed based on C as the following,

$$\overline{C} = C - l_t \tag{3.8}$$

The use of $\overline{U}$ and $\overline{C}$ instead of U and C in the pressure vector is to take into account of the grid speed so that the flux will transit from subsonic to supersonic smoothly. When the grid is stationary, $l_t = 0$, $\overline{C} = C$, $\overline{U} = U$.

The pressure splitting coefficient is:

$$\mathscr{P}^{\pm}_{L,R} = \frac{1}{4}\left(M_{L,R} \pm 1\right)^2 \left(2 \mp M_L\right) \tag{3.9}$$

The LDE scheme is simpler and more CPU efficient than the Roe scheme due to no matrix operation.

3.2 The Fifth-Order WENO Scheme

The interface flux, $E_{i+\frac{1}{2}} = E(Q_L, Q_R)$, is evaluated by determining the conservative variables Q_L and Q_R using fifth-order WENO scheme [31]. For example,

$$\left(Q_L\right)_{i+\frac{1}{2}} = \omega_0 q_0 + \omega_1 q_1 + \omega_2 q_2 \tag{3.10}$$

where

$$\begin{aligned} q_0 &= \tfrac{1}{3}Q_{i-2} - \tfrac{7}{6}Q_{i-1} + \tfrac{11}{6}Q_i \\ q_1 &= -\tfrac{1}{6}Q_{i-1} + \tfrac{5}{6}Q_i + \tfrac{1}{3}Q_{i+1} \\ q_2 &= \tfrac{1}{3}Q_i + \tfrac{5}{6}Q_{i+1} - \tfrac{1}{6}Q_{i+2} \end{aligned} \tag{3.11}$$

$$\omega_k = \frac{\alpha_k}{\alpha_0 + \ldots + \alpha_{r-1}} \tag{3.12}$$

$$
\begin{aligned}
&\alpha_k = \tfrac{C_k}{\varepsilon + IS_k},\ k = 0, \ldots, r-1 \\
&C_0 = 0.1,\ C_1 = 0.6,\ C_2 = 0.3 \\
&IS_0 = \tfrac{13}{12}\left(Q_{i-2} - 2Q_{i-1} + Q_i\right)^2 + \tfrac{1}{4}\left(Q_{i-2} - 4Q_{i-1} + 3Q_i\right)^2 \\
&IS_1 = \tfrac{13}{12}\left(Q_{i-1} - 2Q_i + Q_{i+1}\right)^2 + \tfrac{1}{4}\left(Q_{i-1} - Q_{i+1}\right)^2 \\
&IS_2 = \tfrac{13}{12}\left(Q_i - 2Q_{i+1} + Q_{i+2}\right)^2 + \tfrac{1}{4}\left(3Q_i - 4Q_{i+1} + Q_{i+2}\right)^2
\end{aligned}
\tag{3.13}
$$

where, ε is originally introduced to avoid the denominator becoming zero and is supposed to be a very small number. In [31], it is observed that IS_k will oscillate if ε is too small and also shift the weights away from the optimal values in the smooth region. The higher the ε values, the closer the weights approach the optimal values, C_k, which will give the symmetric evaluation of the interface flux with minimum numerical dissipation. When there are shocks in the flow field, ε can not be too large to maintain the sensitivity to shocks. In [31], $\varepsilon = 10^{-2}$ is recommended for the transonic flow with shock waves.

The viscous terms are discretized by a conservative fourth-order accurate finite central differencing scheme developed by Shen et al [31]. This central differencing scheme is constructed to how the stencil width within the stencil width of the WENO scheme.

$$
\frac{\partial R}{\partial \xi}|_i = \tilde{R}_{i+1/2} - \tilde{R}_{i-1/2} \tag{3.14}
$$

where

$$
\tilde{R}_{i-1/2} = \frac{1}{24\Delta\xi}\left(-R_{i+1/2} + 26R_{i-1/2} - R_{i-3/2}\right) \tag{3.15}
$$

$$
R_{i-1/2} = \left[\left(\xi_x \tau_{xx}\right) + \left(\eta_y \tau_{xy}\right) + \left(\zeta_z \tau_{xz}\right)\right]_{i-1/2}
$$

$$
\begin{aligned}
(\tau_{xx})_{i-1/2} = \ & \mu|_{i-1/2}\{\tfrac{4}{3}\left[(\xi_x \tfrac{\partial u}{\partial \xi})|_{i-1/2} + (\eta_x \tfrac{\partial u}{\partial \eta})|_{i-1/2} + (\zeta_x \tfrac{\partial u}{\partial \zeta})|_{i-1/2}\right] \\
& -\tfrac{2}{3}[(\xi_y \tfrac{\partial v}{\partial \xi})|_{i-1/2} + (\eta_y \tfrac{\partial v}{\partial \eta})|_{i-1/2} + (\zeta_y \tfrac{\partial v}{\partial \zeta})|_{i-1/2} \\
& (\xi_z \tfrac{\partial w}{\partial \xi})|_{i-1/2} + (\eta_z \tfrac{\partial w}{\partial \eta})|_{i-1/2} + (\zeta_z \tfrac{\partial w}{\partial \zeta})|_{i-1/2}]\}
\end{aligned}
\tag{3.16}
$$

If R in Eq.(3.15) can be approximated with the accuracy order not lower than 4th order,

the Taylor expansion analysis of (3.14) and (3.15) will give

$$\tilde{R}_{i+1/2} - \tilde{R}_{i-1/2} = R^{'}(\xi_i) + O(\Delta\xi^4)$$

Where the 4th order accuracy is achieved.

In order to achieve the highest order accuracy of R_I ($I = i-3/2, i-1/2, i+1/2$) in a least stencil not wider than the total width of the WENO stencils, for example, the stencil $S = (x_{i+r}, x_{i+r+1}, \cdots, x_{i+s})$ for all $\frac{\partial u}{\partial \eta}|_I$, $I = i-3/2, i-1/2, i+1/2$, we give the following formulas,

$$\mu_I = \sum_{l=m}^{n} C_l^I \mu_{i+l},\ m = -2, n = 1, \tag{3.17}$$

$$\frac{\partial u}{\partial \xi}|_I = \frac{1}{\Delta\xi} \sum_{l=r}^{s} D_l^I u_{i+l},\ r = -3, s = 2, \tag{3.18}$$

$$\frac{\partial u}{\partial \eta}|_I = \sum_{l=m}^{n} C_l^I \frac{\partial u}{\partial \eta}|_{i+l,j},\ m = -2, n = 1, \tag{3.19}$$

where

$$\frac{\partial u}{\partial \eta}|_{i,j} = \frac{1}{\Delta\eta} \sum_{l=p}^{q} C_l^c u_{i,j+l},\ p = -2, q = 2, \tag{3.20}$$

The other terms are determined similarly.

By choosing different ranges for $(m,n), (r,s), (p,q)$ and different coefficients C_l^I, D_l^I, C_l^c, one can obtain the different order accuracy of the viscous terms.

One principle of choosing $(m,n), (r,s), (p,q)$ is to ensure the approximation of $\frac{\partial R}{\partial \xi}|_i$ (Eq.(3.14))is a central differencing. $(m,n) = (-2,1), (r,s) = (-3,2), and\ (p,q) = (-2,2)$, and the coefficients C_l^I, D_l^I, C_l^c are given in Tables 3.1-3.3.

Table 3.1: The coefficients of C_l^I

I	C_{-2}^I	C_{-1}^I	C_0^I	C_1^I
$i-3/2$	5/16	15/16	-5/16	1/16
$i-1/2$	-1/16	9/16	9/16	-1/16
$i+1/2$	1/16	-5/16	15/16	5/16

Table 3.2: The coefficients of D_l^I

I	D_{-3}^I	D_{-2}^I	D_{-1}^I	D_0^I	D_1^I	D_2^I
$i-3/2$	71/1920	-141/128	69/64	1/192	-3/128	3/640
$i-1/2$	-3/640	25/384	-75/64	75/64	-25/384	3/640
$i+1/2$	-3/640	3/128	-1/192	-69/64	141/128	-71/1920

3.3 Implicit Time Integration

The time dependent governing equations are solved using dual time stepping method suggested by Jameson [41]. To achieve high convergence rate, the implicit pseudo time marching scheme is used with the unfactored Gauss-Seidel line relaxation. The physical temporal term is discretized implicitly using a three point, backward differencing as the following (The prime is omitted hereafter for simplicity):

$$\frac{\partial \mathbf{Q}}{\partial t} = \frac{3\mathbf{Q^{n+1}} - 4\mathbf{Q^{n}} + \mathbf{Q^{n-1}}}{2\Delta t} \tag{3.21}$$

where $n-1$, n and $n+1$ are three sequential time levels, which have a time interval of Δt. The first-order Euler scheme is used to discretize the pseudo temporal term. The semi-discretized equations of the governing equations are finally given as the following:

$$\left[\left(\frac{1}{\Delta\tau} + \frac{1.5}{\Delta t}\right) I - \left(\frac{\partial R}{\partial \mathbf{Q}}\right)^{n+1,m}\right] \delta\mathbf{Q^{n+1,m+1}} = \mathbf{R^{n+1,m}} - \frac{\mathbf{3Q^{n+1,m}} - \mathbf{4Q^{n}} + \mathbf{Q^{n-1}}}{\mathbf{2\triangle t}} \tag{3.22}$$

where the $\Delta\tau$ is the pseudo time step, R is the net flux evaluated on a grid point using the fifth-order WENO scheme and the fourth-order central differencing scheme [31].

Table 3.3: The coefficients of C_l^c

C^c_{-2}	C^c_{-1}	C^c_0	C^c_1	C^c_2
1/12	-8/12	0	8/12	-1/12

Chapter 4

Delayed-Detached-Eddy Simulation and Shock/Wave Turbulent Boundary Layer Interaction

Turbulence is a physical problem that is delineated by its highly chaotic nature and as a result there is no general solution available. In consequence there are several turbulent models that have been developed for a close resemblance to this phenomenon. The present work makes use of the delayed-detached-eddy simulation model and compares it to its predecessors the Sparlat and Allmaras one-equation model and the detached-eddy simulation model.

4.1 3D Subsonic Flat Plate

The subsonic flat plate is used to validate the performance of the DDES scheme. The mesh size is $181 \times 81 \times 65$. The y^+ of the first cell center to the wall is kept less than 1.0. The mesh can be observed in Fig. 4.1 and Fig. 4.2. The Reynolds number is 4×10^6 based on the length of the plate. The inlet Mach number is 0.5.

As shown in Fig. 4.3, the computational results of the DDES scheme agree well with the law of the wall. They are slightly better than the results using S-A model alone in the transition region from the linear viscous sublayer to log layer.

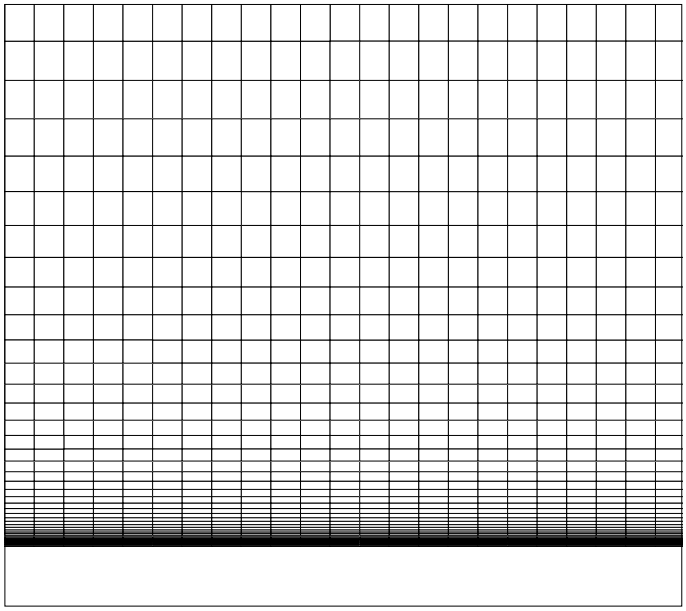

Figure 4.1: 2D view of the mesh for subsonic flat plate

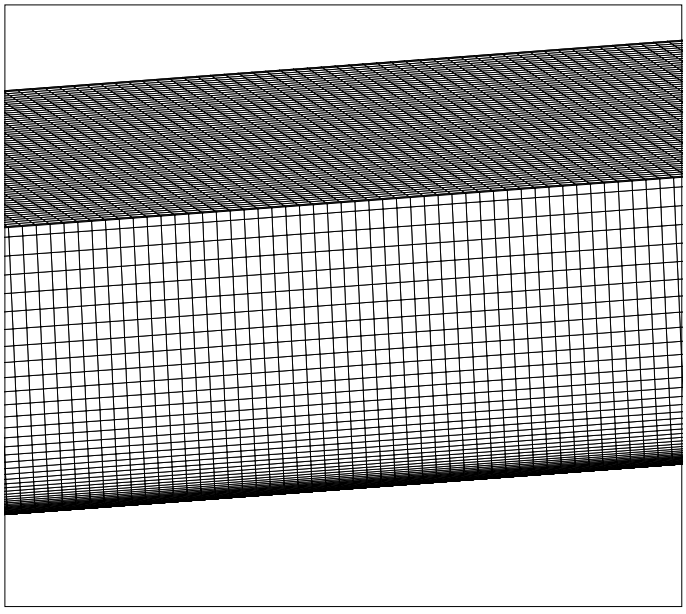

Figure 4.2: 3D view of the mesh for the subsonic flat plate

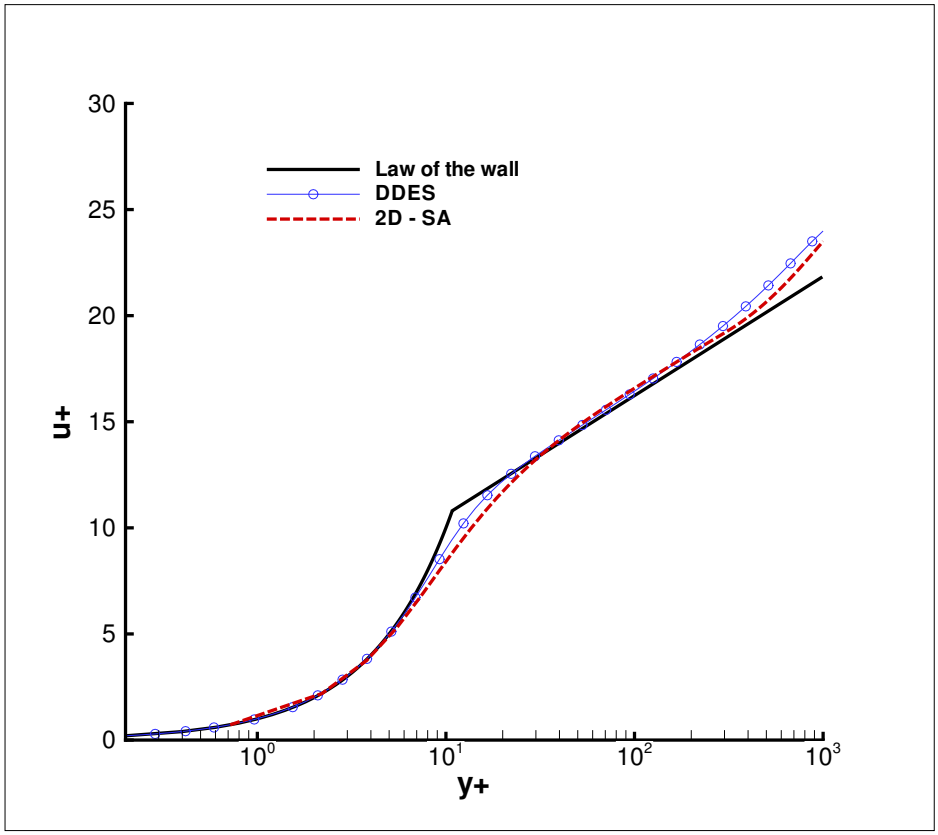

Figure 4.3: Law of the wall of a subsonic flat plate

Chapter 5

3D Transonic Channel Flow

5.1 Geometry

In this thesis, the flow in a transonic channel is simulated, using both DES and DDES models, to study the shock wave/turbulent boundary layer interaction, which is analyzed experimentally in reference [42]. The channel is made of two straight side walls, a straight top wall, and a varying shape in span-wise direction for a bottom wall. The section tested on [2] has an entrance of 100mm in height by 120mm in width. Fig. 5.1 shows the topology of the duct's shape.

5.2 Inlet and Boundary Conditions

For the computation, the inlet boundary conditions are set as fixed total pressure, total temperature and flow angles. At the outlet a fixed static pressure is specified. On the walls, the boundary conditions are set as no-slip adiabatic wall boundary condition. The flow for both DES and DDES models is calculated with a Reynolds number of 11.3×10^6 based on the throat's height and an inlet Mach number of 0.502.

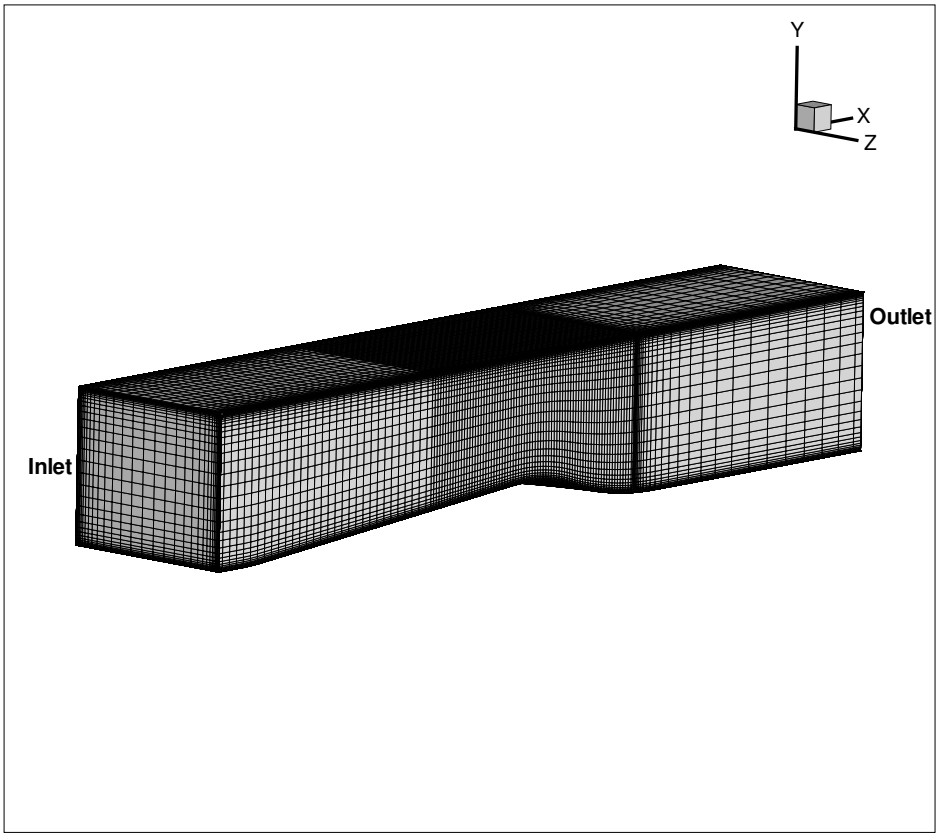

Figure 5.1: The computational grid of the transonic channel

5.3 CFD Simulation

5.3.1 Mesh Generation

Two mesh sizes are used for the DES calculation of $91 \times 61 \times 61$ and $136 \times 91 \times 91$, and three mesh sizes are used for the DDES calculation of $91 \times 61 \times 61$, $136 \times 91 \times 91$ and $211 \times 91 \times 91$. The meshes are mostly uniformly distributed in the horizontal direction except for the bump area, where the mesh is clustered to better observe the shock wave. In the same way, the clustering also appears near the four walls of the duct to resolve the boundary layer. Fig. 5.1 shows the 3D mesh of the transonic channel.

5.3.2 CFD Pre-Processing

A non-dimensional time step of 0.05 was used for the cases. The non-dimensional time is defined as $\bar{t} = \frac{t}{D/U_\infty}$, where D is the throat height. The computation begins with a uniform flow field. The convergence history within a typical physical time step is shown in Fig. 5.2, which the residual reduced by 2-3 orders of magnitude.

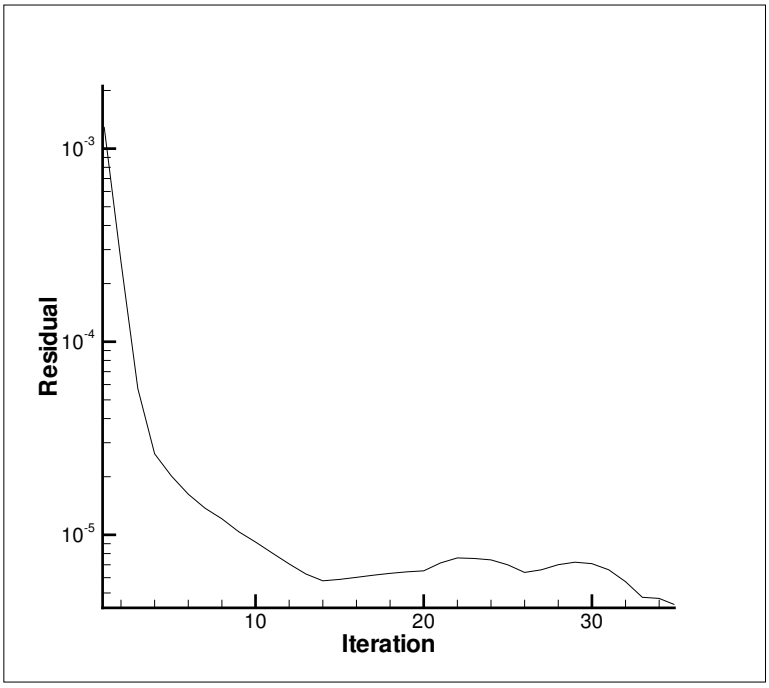

Figure 5.2: Convergence history within a typical time step for transonic duct

5.4 Results

Fig. 5.3 and Fig. 5.4 show the computed instant shock wave structure shown by Mach contours at 3 span-wise planes for the DES and DDES simulations respectively. Fig. 5.5 shows the result of the Mach number contours for the experiment [2] which can be compared to those of Fig. 5.3 and Fig. 5.4. The location of the planes from the back wall are $Z = 60mm$, $Z = 75mm$ and $Z = 90mm$, with the one located at $Z = 60mm$ being the central plane of the channel. In order to achieve the location of the shock to be the same as in the experiment,

the value of $\frac{p_{out}}{p_t} = 0.59$ is used for both DES and DDES. Both the DES and DDES simulations have results in the shock wave structure very similar to that of the experiment, as shown in Fig. 5.5.

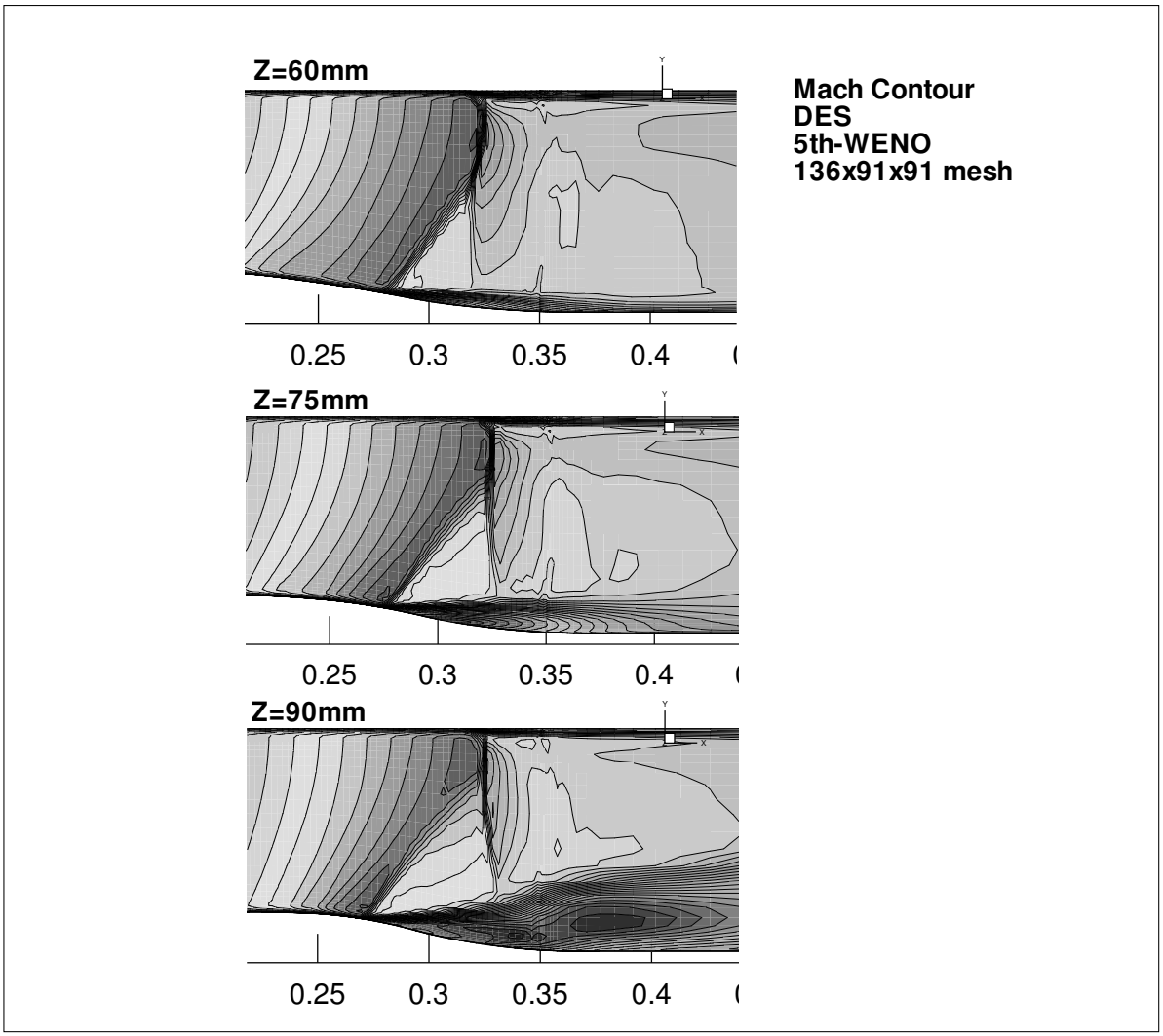

Figure 5.3: Transonic duct Mach number contours for DES

Compare the DES and DDES results at the plane $Z = 60mm$, the boundary layer of DDES is thinner than that of DES and agrees better with the experiment. The major difference between the results of DES and DDES simulations can be seen in plane $Z = 90mm$, where DES shows a thick layer with an area of separation significantly larger than the experiment. When looking at the DDES results, the separation is substantially reduced and agrees better with the experiment.

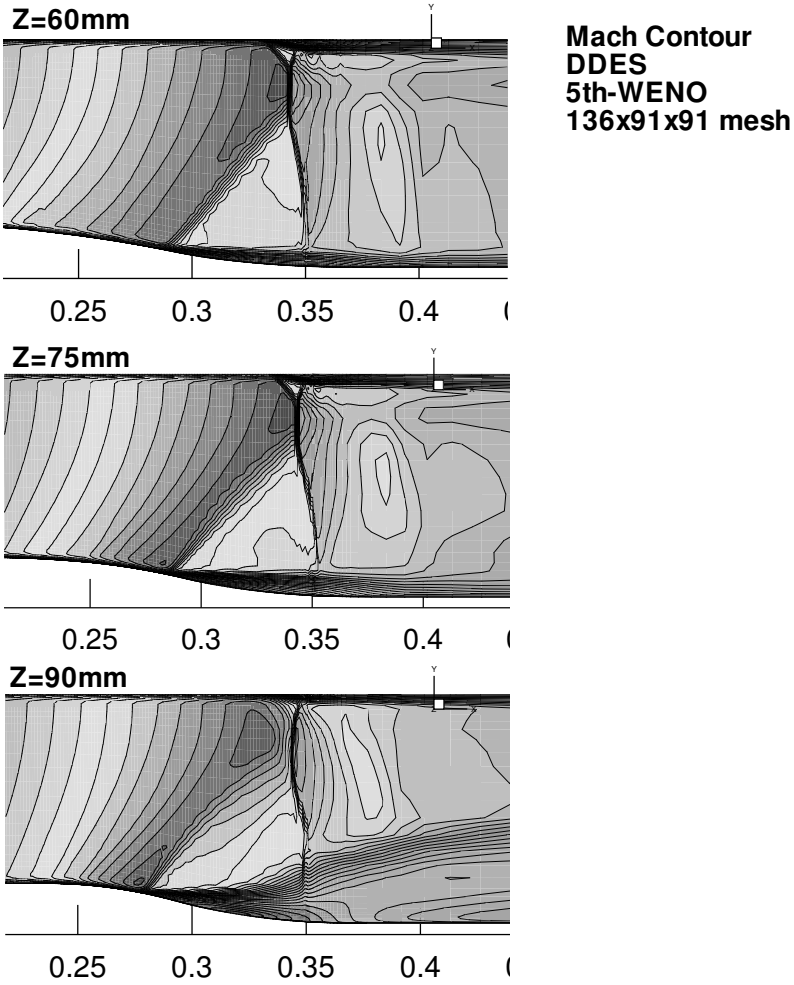

Figure 5.4: Transonic duct Mach number contours for DDES

The surface shear stress flow are also plotted in this study and are found in Fig. 5.6 and Fig. 5.7. They show three faces of the channel, the top wall and both of the side walls. The results agree well with the experiment [2] observed in Fig. 5.8, DDES having a better agreement which can be observed on side A of the channel on the area close to the top and bottom walls.

The mesh refinement study with the mesh sizes mentioned above shows that DES is mesh dependent (grid density), given that the finner the mesh near the walls, the less agreement with the experimental results. This is then resolved with the use of DDES as indicated by Sparlat [27].

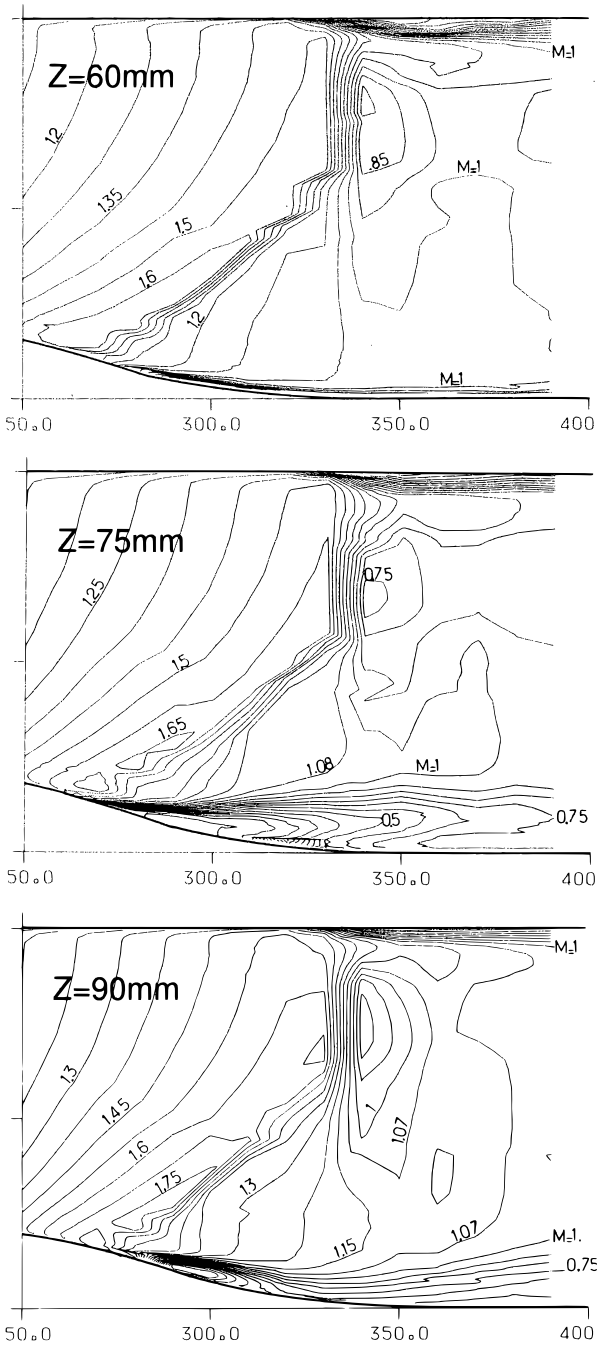

Figure 5.5: Transonic duct Mach number contours from experiment

Fig 5.9 shows a plot of the computational isentropic Mach numbers on the top wall on plane $Z = 60mm$ of the transonic channel compared to the experiment [2]. The computed values are slightly lower than those of the experiment because the strength of the shock wave is not as strong which could result as a problem of the mesh density near the boundary

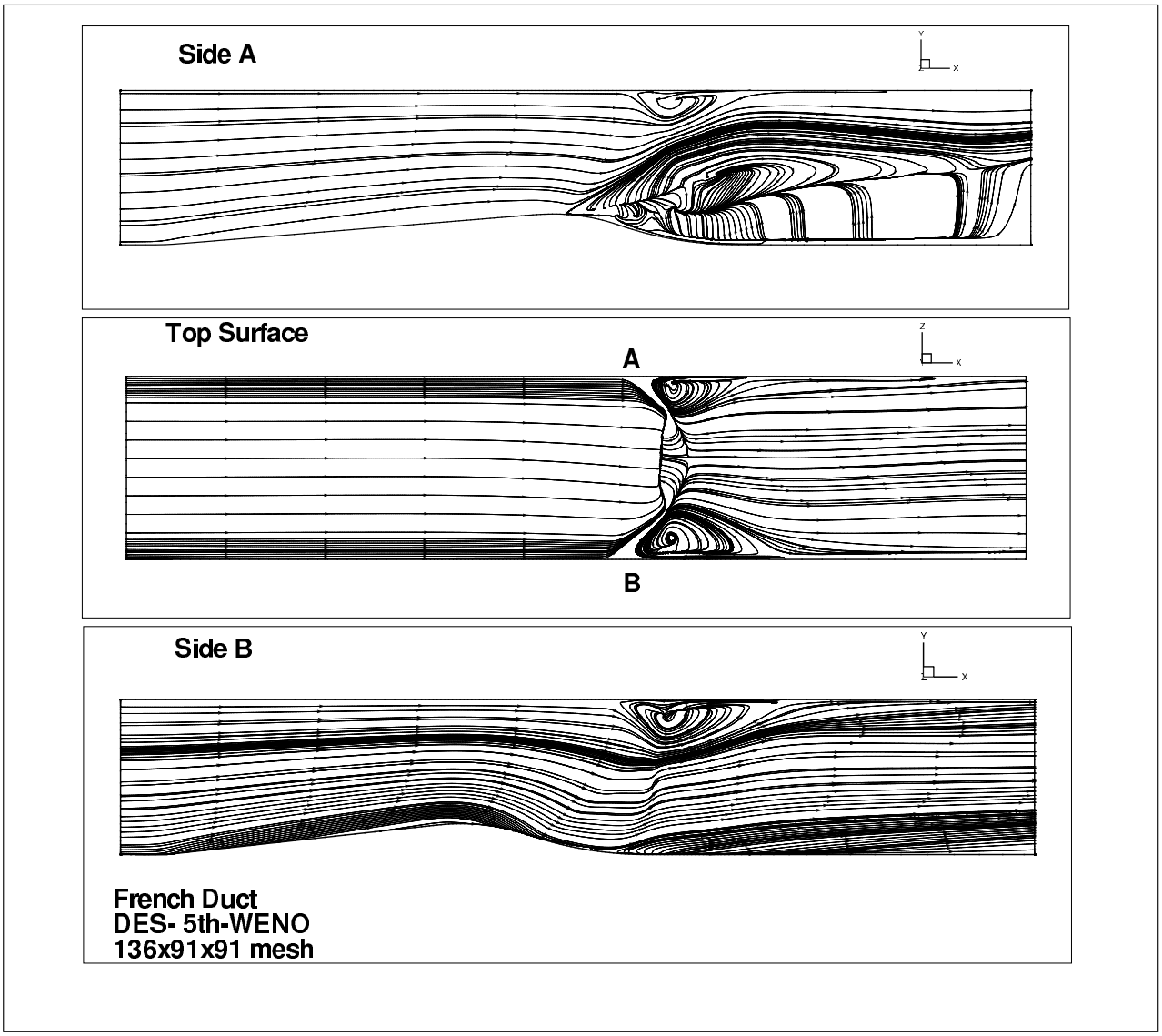

Figure 5.6: Transonic duct surface shear stress lines on walls for DES

layer. The plot also shows that the finner the mesh for the DDES gives more accurate results, which for DES the opposite occurs and therefore resolved by the implementation of DDES. The similarity in the DDES solutions for the $136 \times 91 \times 91$ and $211 \times 91 \times 91$ meshes show the convergency of the results.

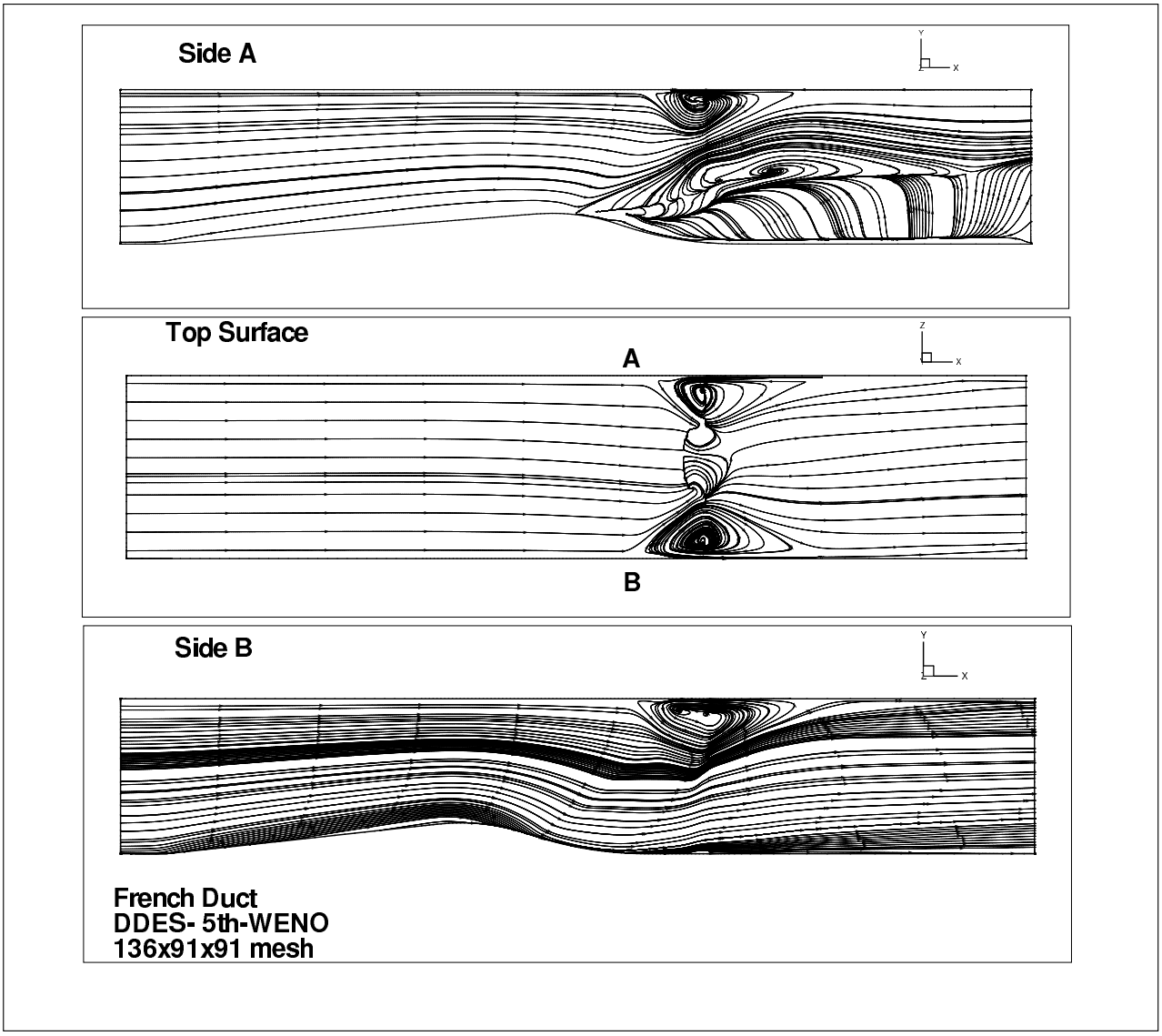

Figure 5.7: Transonic duct surface shear stress lines on walls for DDES

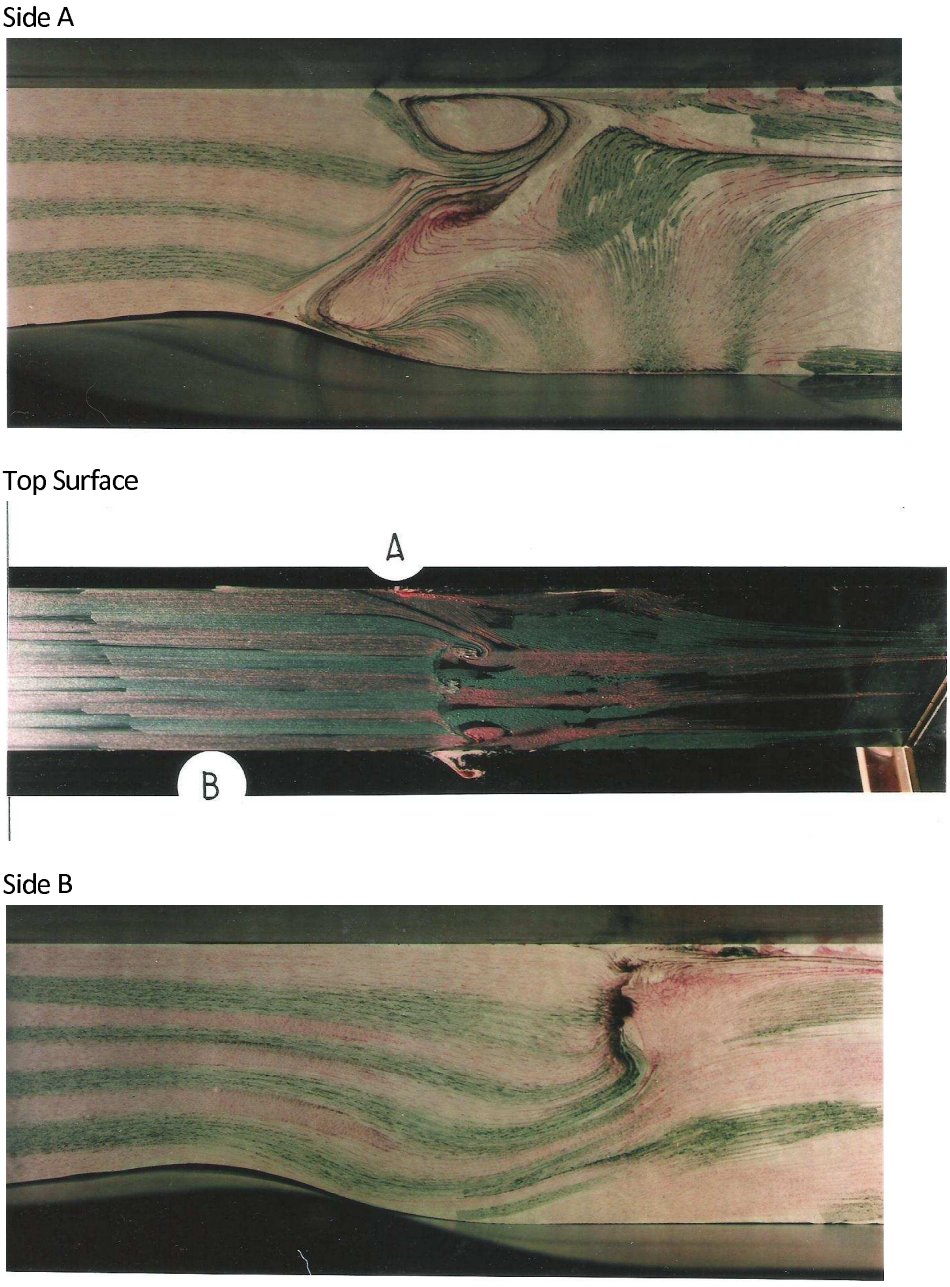

Figure 5.8: Transonic duct surface experimental shear stress for top, side A and side B walls [2]

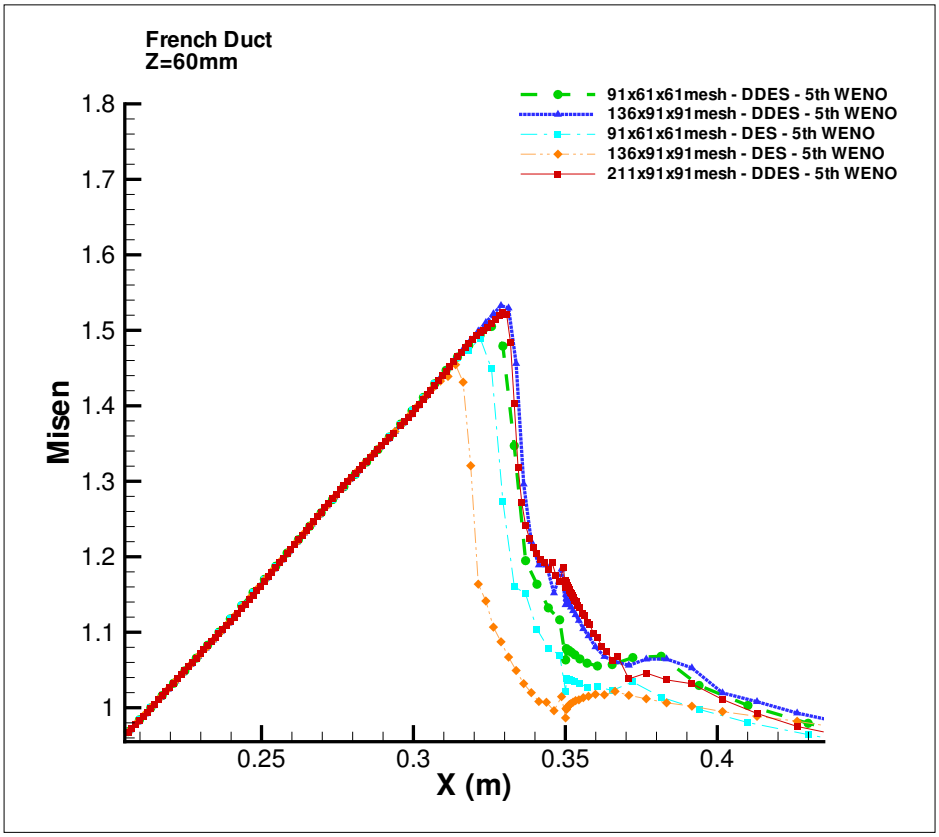

Figure 5.9: Isentropic Mach number on top wall of transonic duct at plane Z=60mm, experiment data [2]

Chapter 6

Transonic Inlet-Diffuser

6.1 Geometry

The flow in a transonic inlet-diffuser is simulated, using SA, DES and DDES models, to study the shock wave/turbulent boundary layer interaction, which is described experimentally in reference [43]. The mesh is a 3D grid, with a straight bottom wall, two converging straight side walls, and a varying shape in span-wise direction for a top wall. Fig. 6.1 shows the topology of the inlet-diffuser's shape.

6.2 Inlet and Boundary Conditions

For the computation, the inlet boundary conditions are set as fixed total pressure, total temperature and flow angles, the same way as it is defined for the transonic channel flow. At the outlet a fixed back pressure is specified, which equals to 0.72 times of the inlet total pressure. On the walls, the boundary conditions are set as no-slip adiabatic wall boundary condition. The flow for both DES and DDES models is calculated with a Reynolds number of 8.39645×10^5 based on the throat's height and a Mach number of 0.9.

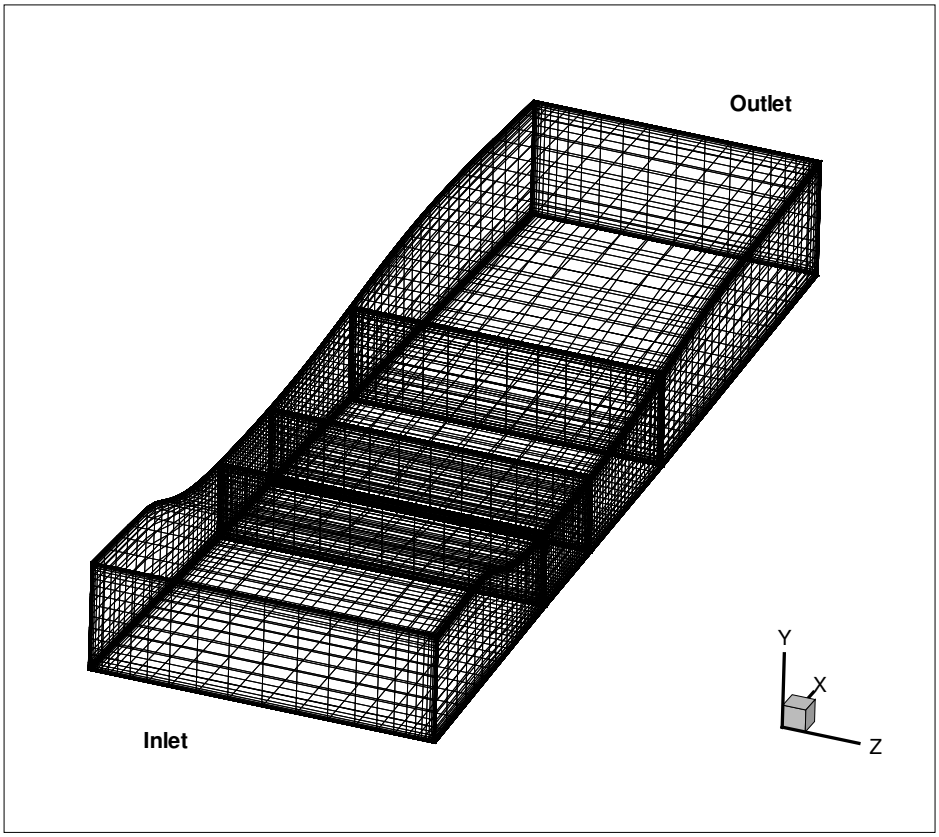

Figure 6.1: The computational grid of the transonic inlet-diffuser

6.3 CFD Simulation

6.3.1 Mesh Generation

The baseline mesh size is $81 \times 51 \times 51$ with a y+ lower than 3. The mesh is refined in both horizontal and vertical directions to $101 \times 61 \times 51$, but the results have little variation. The mesh is mostly uniformly distributed in the horizontal direction except for the throat area, where it is finner to better catch the shock wave. The mesh distribution can be observed in Fig. 6.1. At the end, three different meshes with the dimensions of the baseline are generated which they differ in the angle in which the side walls converge towards each other. This is performed because of the way the experimental setup is conducted and the 2D computational results available. The three angles of convergence at which the simulation is performed, taking the x-horizontal as reference, are $\theta = 1.10$, $\theta = 1.31$, and $\theta = 1.67$.

6.3.2 CFD Pre-Processing

A non-dimensional time step of 0.05 was used for all the cases. The computation begins with a uniform flow field. The convergence history within a typical physical time step is shown in Fig. 6.2.

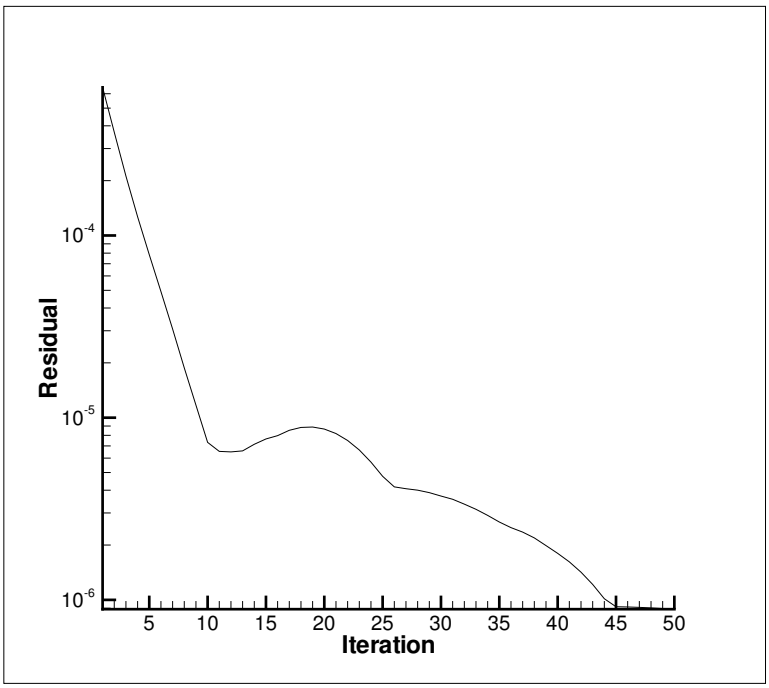

Figure 6.2: Convergence history within a typical time step for transonic inlet-diffuser

6.4 Results

Fig. 6.3, Fig. 6.4 and Fig, 6.5 show the mach contours computed using the SA scheme, DES scheme, and DDES scheme, respectively. The three different discretization schemes show discrepancies between each other which denotes how turbulence modeling is a critical factor for the prediction accuracy of the shock wave/turbulent boundary layer interaction. Observing the figures, the shock location varies across convergence angles, as well as schemes. The shock wave is less visible, if not inexistent on the DES cases. Given that DES was designed to treat the entire boundary layer using a RANS model, this incorrect behav-

ior in this case is caused by a fine mesh which grid spacing much smaller than the boundary layer thickness locating the RANS/LES transition within the boundary layer itself. Then comparing the DES model with the DDES model, there is an improvement based on the only factor that the shock wave that is visible with SA, is visible again when computed with DDES, because of a better definition of the boundary layer, which is independent from the mesh definition on the wall.

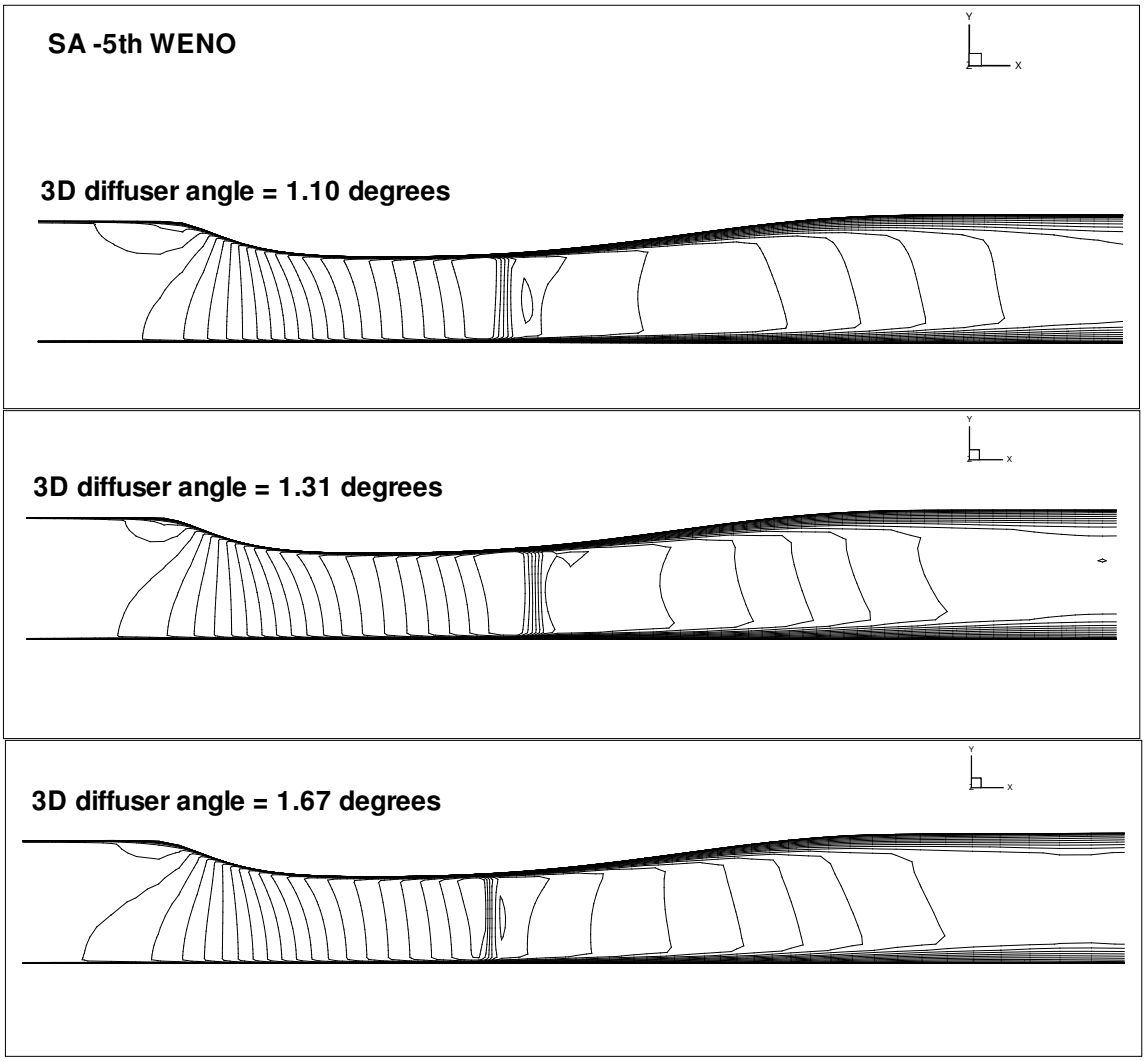

Figure 6.3: Mach contours of the transonic inlet-diffuser for SA model

Fig. 6.6, Fig. 6.7 and Fig, 6.8 show the pressure contours computed using the SA scheme, DES scheme, and DDES scheme, respectively. These contours show again the same results as presented by the mach countours, although this time for the DDES case for

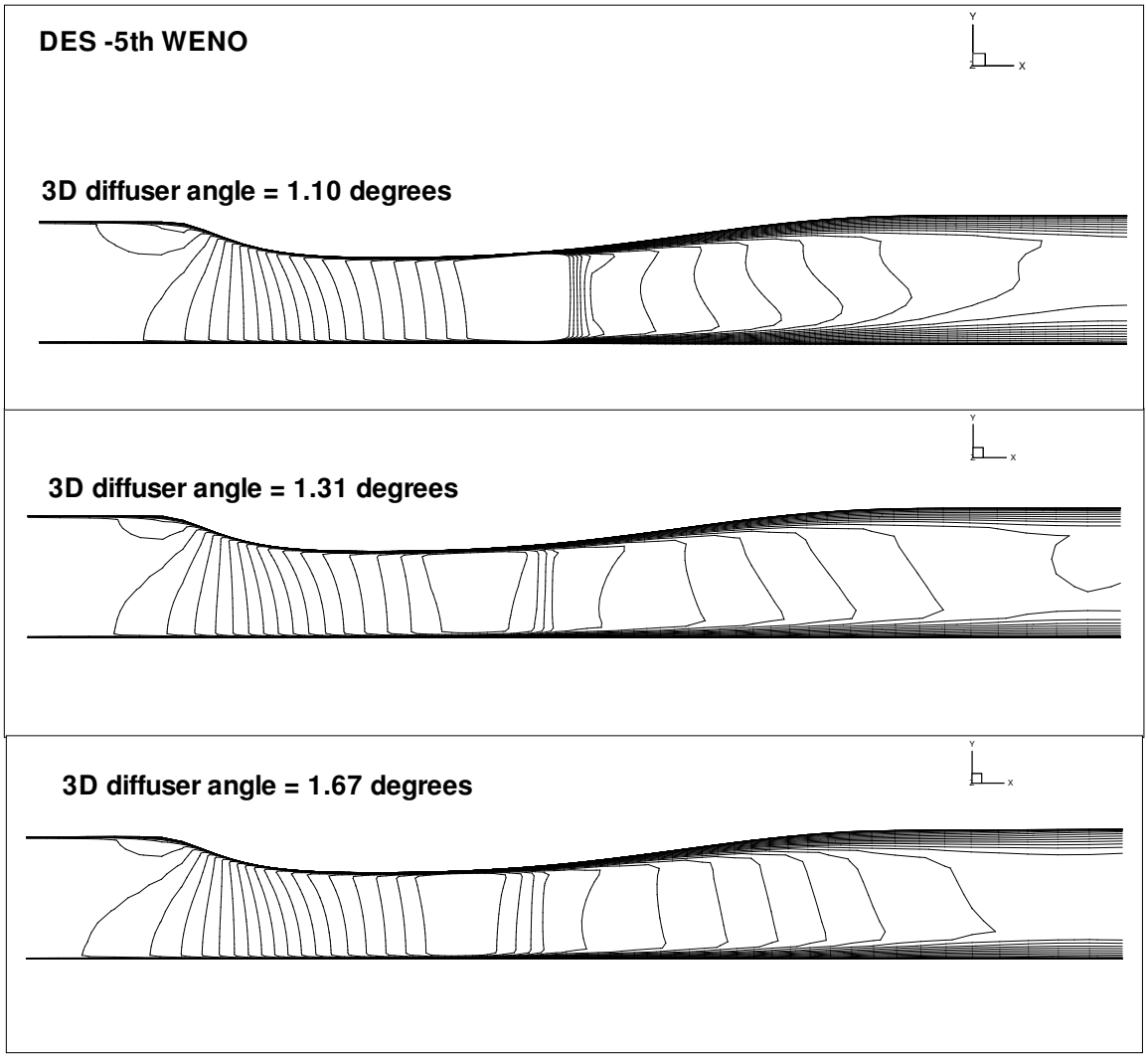

Figure 6.4: Mach contours of the transonic inlet-diffuser for DES model

an angle of 1.31, the curved α-shock can almost be captured.

Fig. 6.9, Fig. 6.10 and Fig, 6.11 show the pressure distribution computed on the top wall compared with experiment using the SA scheme, DES scheme, and DDES scheme, respectively. The computational results are also compared with those calculated usind the DDES scheme but on a 2D geometry. The 2D geometry results practically mimic the experimental ones, assuming that the 3D results would do the same. This is not the case, given that for all three schemes it can been seen in the figures that the shock wave is not nearly strong enough to provide the expected results. As a consequence, the angle of convergence is changed and various calculations are performed in search of the experimental

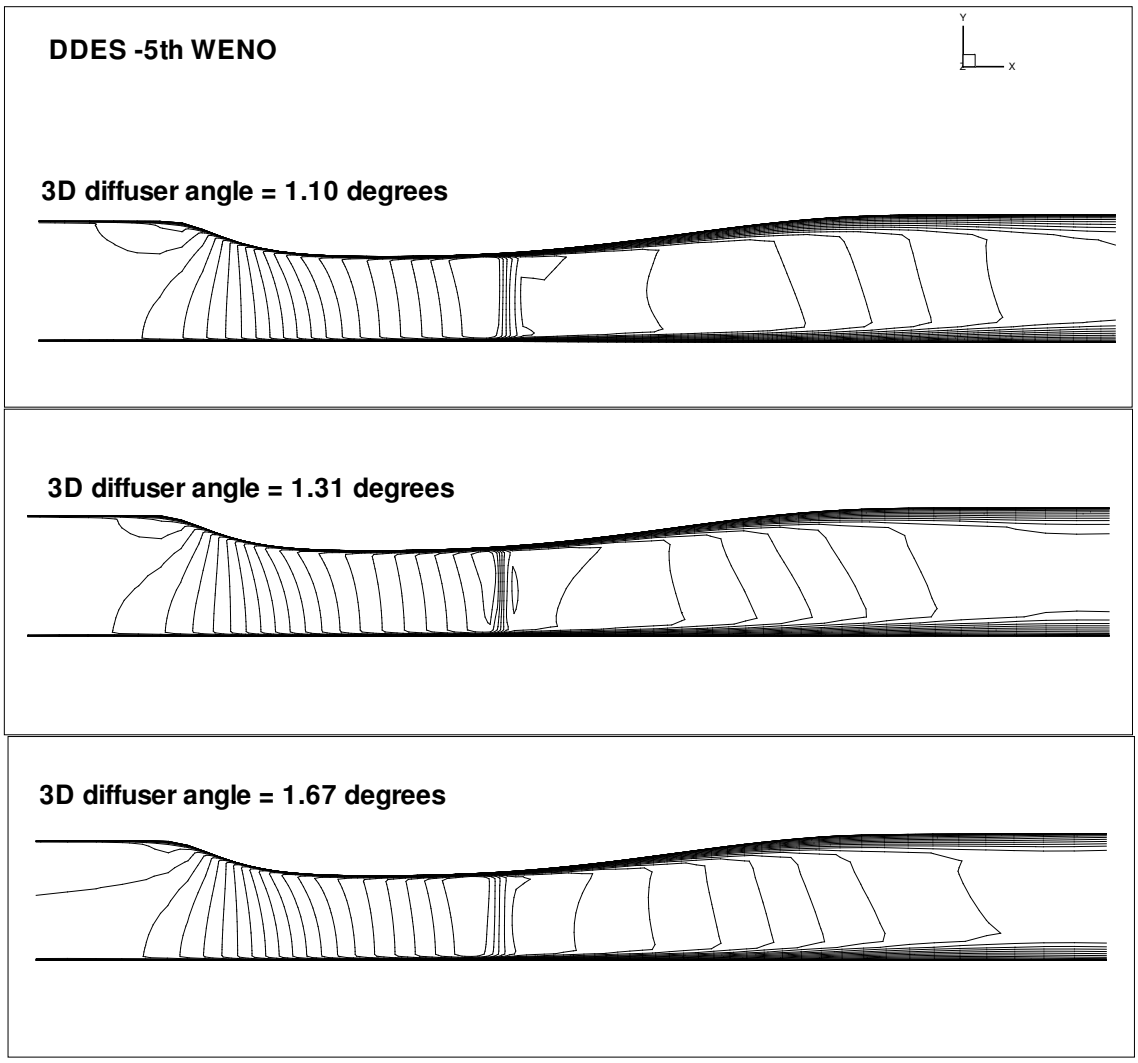

Figure 6.5: Mach contours of the transonic inlet-diffuser for DDES model

solution. Fig. 6.9, Fig. 6.10 and Fig, 6.11 illustrate that the objective is not reached and that further investigation needs to be performed to find the ideal conditions of the 3D mesh to find matching results to the 2D ones.

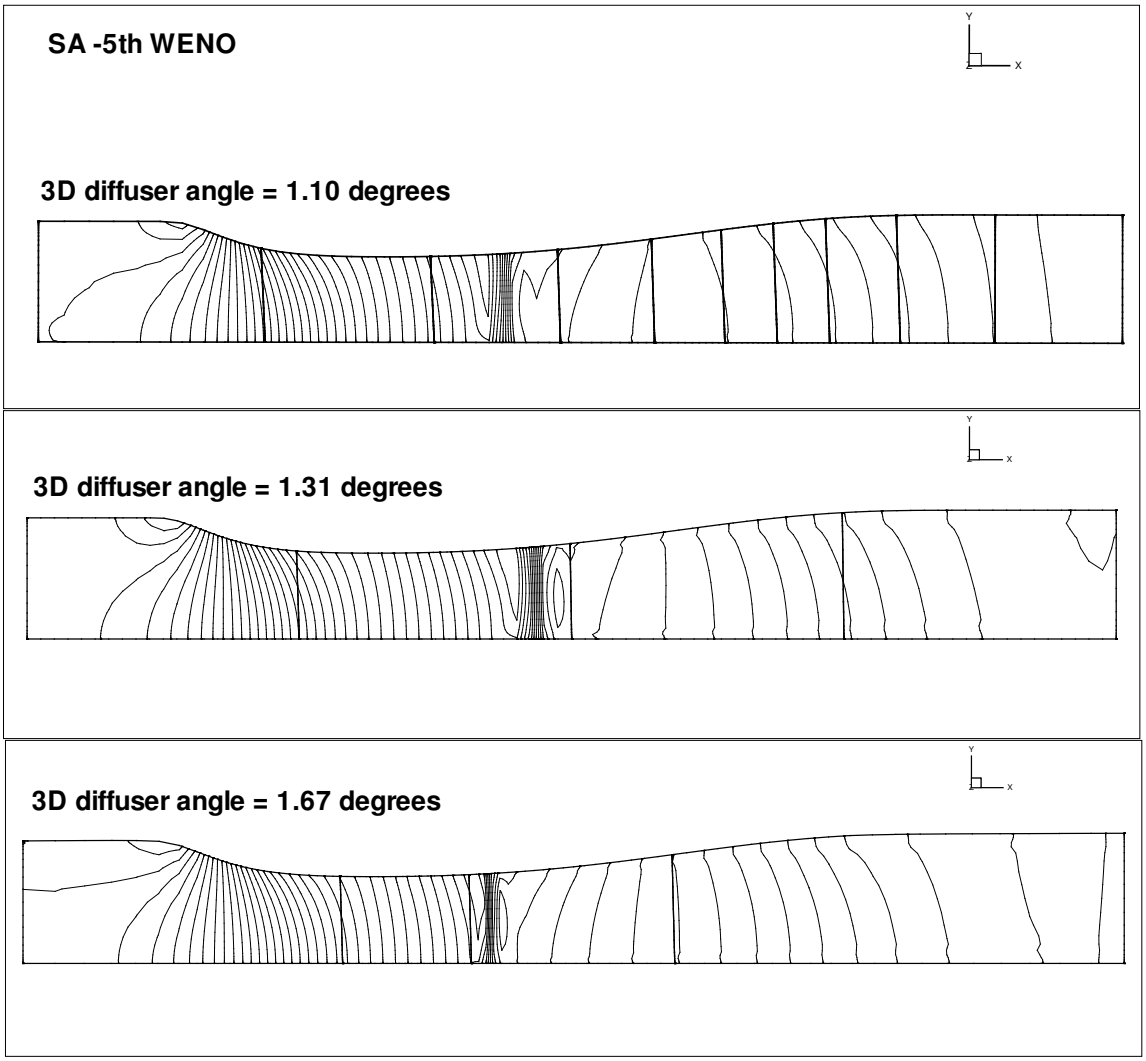

Figure 6.6: Pressure contours of the transonic inlet-diffuser for SA model

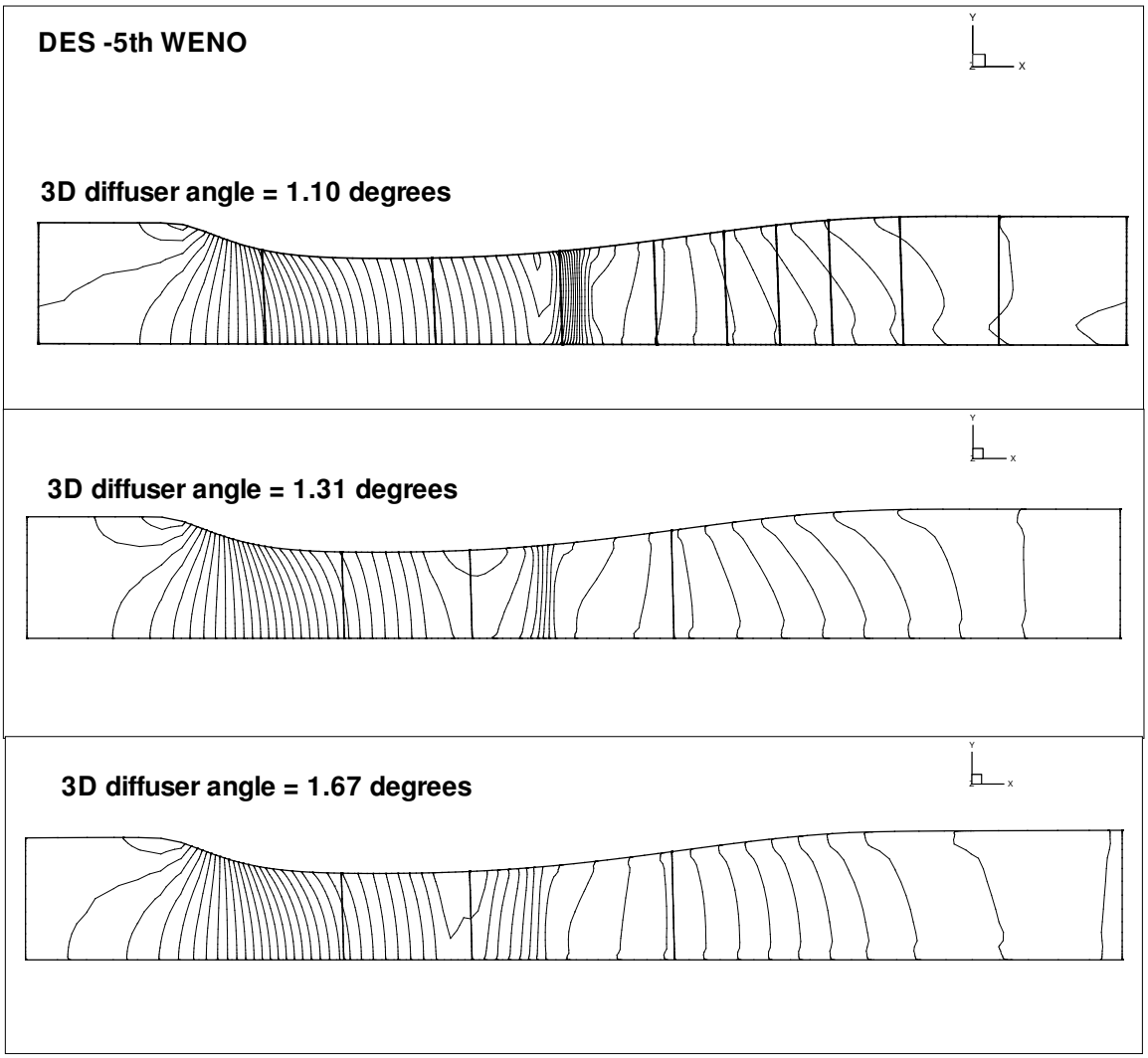

Figure 6.7: Pressure contours of the transonic inlet-diffuser for DES model

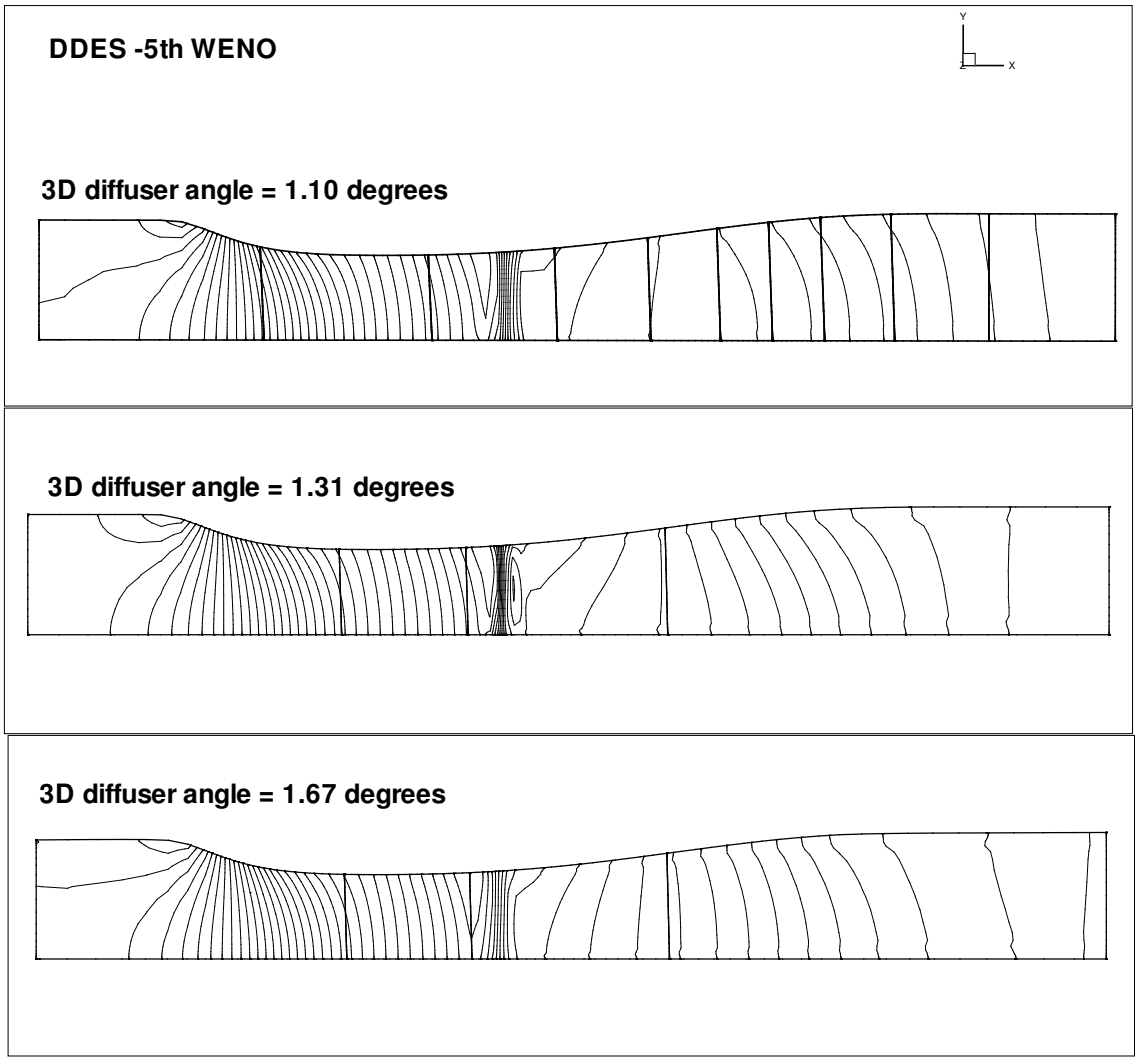

Figure 6.8: Pressure contours of the transonic inlet-diffuser for DDES model

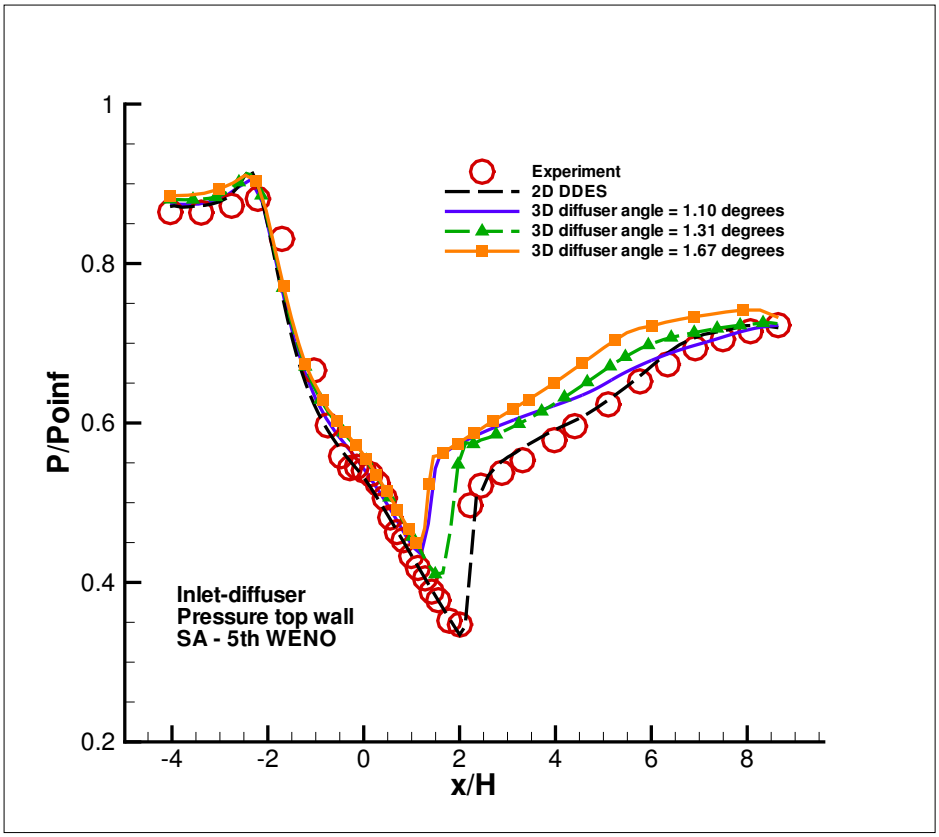

Figure 6.9: Upper wall pressure of the transonic inlet-diffuser for SA model

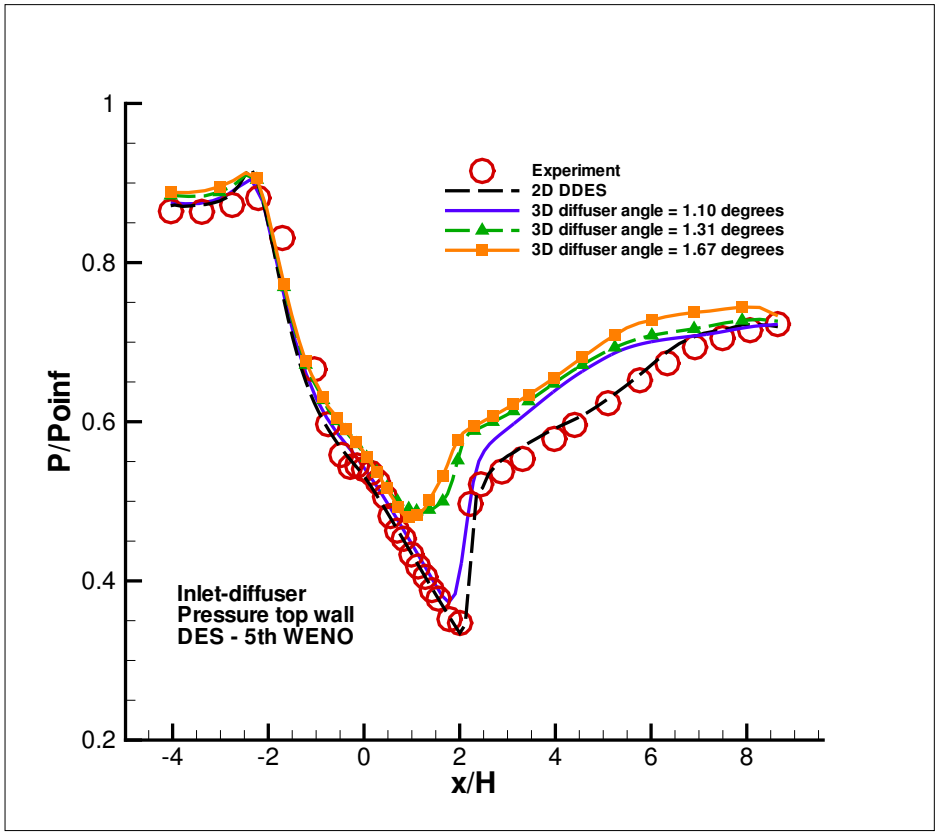

Figure 6.10: Upper wall pressure of the transonic inlet-diffuser for DES model

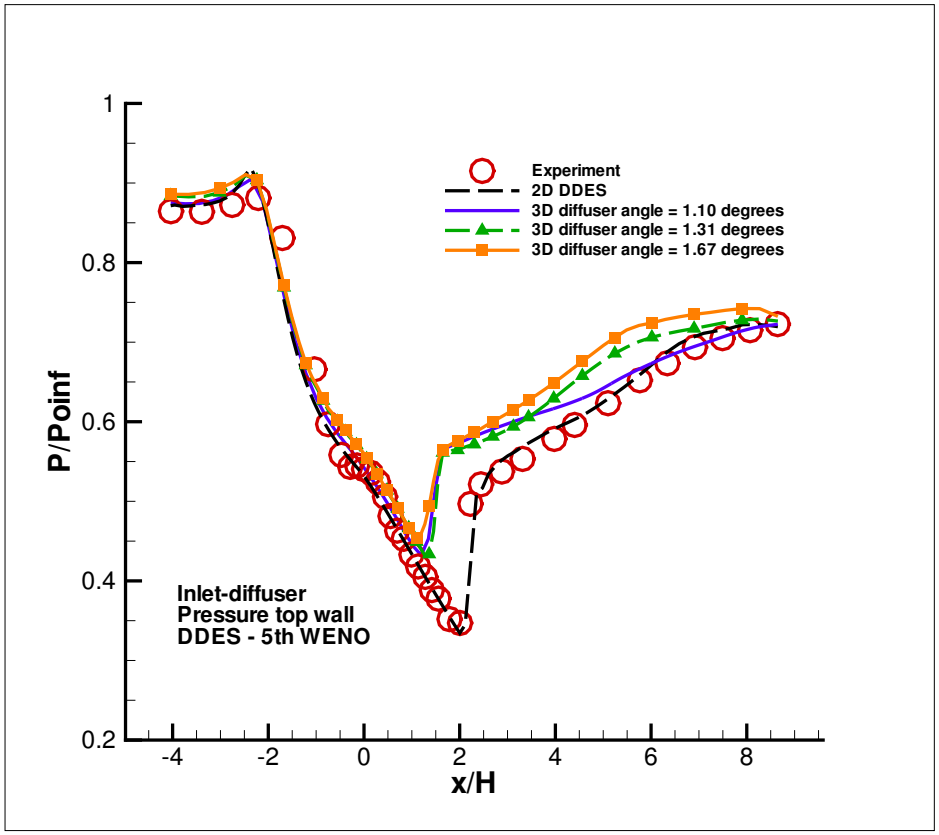

Figure 6.11: Upper wall pressure of the transonic inlet-diffuser for DDES model

Chapter 7

Conclusions

The shock/wave turbulent boundary layer interaction is studied using a DDES simulation with a low diffusion E-CUSP scheme [44] and fifth-order WENO scheme. A 4th order central differencing is used for the viscous terms.

The Delayed-Detached-Eddy Simulation (DDES) was suggested by Spalart in 2006 to fix a problem with the DES model he had previously developed in 1997. The transition from the RANS model to LES in DES is not grid spacing independent, therefore a blending function is introduced to the recently developed DDES model to make the transition from RANS to LES grid spacing independent. The validation of the DDES method is performed by the simulation of the flow field of a 3D subsonic flat plate turbulent boundary layer. The computational results of the DDES scheme agree well with the law of the wall, being slightly better than those of the S-A model.

For a 3D transonic duct with a baseline grid of $136 \times 91 \times 91$, the computed shock/wave structure for three span wise planes agrees better with experiment using DDES compared to the results of DES near the walls of the channel. The computation of mesh refinement indicates that the grid density has significant effects on the results of DES, while being resolved by applying DDES simulation.

For a 3D transonic inlet-diffuser with a baseline grid of $81 \times 51 \times 51$, the DES simula-

tion is not able to predict the location and strength of the shock/wave. Although the DDES simulation does not provide a quite accurate solution, it does give much better results than the ones provided by its predecessor the DES. In order to find the ideal conditions and geometry of the 3D mesh, further investigation remains to be done, so the results can agree as well as the 2D DDES with the experiment.

References

[1] G.-C. Zha, Y. Shen, and B. Wang, "Calculation of Transonic Flows Using WENO Method with a Low Diffusion E-CUSP Upwind Scheme." AIAA Paper 2008-0745, 46th AIAA Aerospace Sciences Meeting, Reno, NV, Jan. 2008.

[2] R. Benay, J. M. Délery, and T. Pot, "Etude expérimentale d'une interaction onde de choc-couche limite en canal tridemensionnel. propriété du champ moyen," Tech. Rep. Rapport Technique no 70/7078 AN, ONERA, 1986.

[3] J. Smagorinsky, "General Circulation Experiments with the Primitive Equations, I. The Basic Experiment," *Monthly Weather Review*, vol. 91, pp. 99–164, 1963.

[4] D. Lilly, "The Presentation of Small-Scale Turbulent in Numerical Simulation Experiments," *IBM Scientific Computing Symp. on Environmental Sciences*, p. 195, 1967.

[5] M. Germano, U. Piomeli, P. Moin, and W. Cabot, "A Dynamic Subgrid-scale Eddy Viscosity Model," *Physics of Fluids A*, vol. 3, pp. 1760–1765, July 1991.

[6] U. Piomeli, W. Cabot, P. Moin, and S. Lee, "Subgrid Scale Backscatter in Turbulent and Transitional Flows," *Physics of Fluids A*, vol. 3, pp. 1766–1771, July 1991.

[7] J. Deardorff, "A Numerical Study of Three Dimensional Turbulent Channel Flow at Large Reynolds Numbers," *Journal of Fluid Mechanics*, vol. 41, pp. 453–480, 1970.

[8] T. Kawamura and K. Kuwahara, "Computation of High Reynolds Number Flow Around a Circular Cylinder with Surface Roughness." AIAA Paper-84-0340, 1984.

[9] F. Grinstein, "Dynamics of Coherent Structures and Transition to Turbulence in Free Square Jet." AIAA Paper-96-0781, 1978.

[10] J. P. Boris, "On Large Eddy Simulation Using Subgrid Turbulence Models, in Whither Turbulence? ," *Turbulence at the Crossroads, edited by J.L. Lumley, New York: Springer-Verlag*, 1990.

[11] J. Boris, F. Grinstein, E. Oran, and R. Kolbe, "New Insights into Large Eddy Simulation," *Journal of Fluid Mechanics*, vol. 41, pp. 453–480, 1970.

[12] Boris, J., " More for LES: A Brief Historical Perspective of MILES," *Implicit Large Eddy Simulation, Editors: F. F. Grinstein, L. G. Margolin, and W. J. Rider*, vol. Cambridge University Press, pp. 9–38, 2007.

[13] Y.-Q. Shen and G.-C. Zha, "Comparison of High Order Schemes for Large Eddy Simulation of Circular Cylinder Flow." Submitted to 47th AIAA Aerospace Sciences Meeting and Exhibit, Jan., 2009.

[14] Y.-Q. Shen and G.-C. Zha, "Comparison of High Order Schemes for Large Eddy Simulation of Circular Cylinder Flow." AIAA-2009-0945, Submitted to Journal of Computational Physics, 2009.

[15] P. Spalart, W.-H. Jou, M. Strelets, and S. Allmaras, "Comments on the Feasibility of LES for Wings, and on a Hybrid RANS/LES Approach." Advances in DNS/LES, 1st AFOSR Int. Conf. on DNS/LES, Greyden Press, Columbus, H., Aug. 4-8, 1997.

[16] P. R. Spalart, "Young-Person's Guide to Detached-Eddy Simulation Grids." NASA/CR-2001-211032, 2001.

[17] P. R. Spalart, "Topics in Detached-Eddy Simulation."

[18] B.-Y. Wang and G.-C. Zha, "Dettached Eddy Simulation of Transonic Airfoil Limited Cycle Oscillation with High Order WENO Scheme." AIAA Paper 2009-1507, the 47th AIAA Aerospace Sciences Meeting and Exhibit, Orlando, Florida, 5 - 8 Jan 2009.

[19] B.-Y. Wang and G.-C. Zha, "Detached-Eddy Simulation of a Co-Flow Jet Airfoil at High Angle of Attack." AIAA Paper 2009-4015, 2009.

[20] A. Tarvin, M. Shur, M. Strelets, and P. Spalart, "Detached-Eddy Simulations Past a Circular Cylinder," *Flow Turbulence and Combustion*, vol. 63, 1999.

[21] J. R. Forsythe, K. A. Hoffmann, and K. D. Cummings, R. M. Squires, "Detached-Eddy Simulations with Compressibility Corrections Applied to Supersonic Axisymmetric Base Flow," *Journal of Fluids Engineering*, vol. 124, 2002.

[22] A. Viswanathan, K. Klismith, J. Forsythe, and K. D. Squires, "Detached-Eddy Simulation around a Forebody at High Angle of Attack." AIAA-2003-0263, 2003.

[23] K. D. Squires, "Detached-Eddy Simulation: Current Status and Perspectives."

[24] K. D. Squires, J. R. Forsythe, and P. R. Spalart, "Detached-Eddy Simulation of the Seperated Flow Around a Forebody Cross-Section."

[25] R. P. Hansen and J. R. Forsythe, "Large and Detached Eddy Simulation of a Circular Cylinder Using Unstructured Grids." AIAA Paper 2003-0775, Jan. 2003.

[26] P. Subbareddy and G. V. Candler, "Numerical Investigations of Supersonic Base Flows Using DES." AIAA Paper 2005-0886, Jan. 2005.

[27] P. Spalart, S. Deck, M. Shur, and K. Squires, "A New Version of Detached-Eddy Simulation, Resistant to Ambiguous Grid Densities," *Theoritical and Computational Fluid Dynamics*, vol. 20, pp. 181–195, 2006.

[28] C. Rumsey, "Successes and Challenges for Flow Control Simulations." AIAA Paper 2008-4311,AIAA 4th Flow COntrol Conference, Seattle, Washington, 23-26 June 2008.

[29] F. Menter and M. Kuntz, "Adaptation of Eddy-Viscosity Turbulence Models to Unsteady Separated Flow Behind Vehilces, *The Aerodynamics of Heavy Vehicles: Trucks, Buses and Trains, Edited by McCallen, R. Browand, F. and Ross, J.* ," *Springer, Berlin Heidelberg New York, 2004*, 2-6 Dec. 2002.

[30] C.-W. Shu, "Essentially Non-Oscillatory and Weighted Essentially Schemesfor Hyperbolic Conservation Laws." NASA/CR-97-206253, 1997.

[31] Y.-Q. Shen, B.-Y. Wang, and G.-C. Zha, "Implicit WENO Scheme and High Order Viscous Formulas for Compressible Flows ." AIAA Paper 2007-4431, 2007.

[32] Z. Hu, "Parallel Computation of Fluid-Structure Interaction Using High Resolution Upwind Schemes." Ph.D. Thesis, University of Miami, May 2005.

[33] P. Spalart and S. Allmaras, "A One-equation Turbulence Model for Aerodynamic Flows." AIAA-92-0439, 1992.

[34] R. P. Hansen and J. Forsythe, "Large and Detached Eddy Simulation of a Circular Cylinder Using Unstructured Grids." AIAA-2003-0775, 2003.

[35] M. Shur, P. Spalart, M. Strelets, and A. Travin, "Detached-Eddy Simulation of an Airfoil at High Angle of Attack", 4th Int. Symp. Eng. Turb. Modelling and Measurements, Corsica." May 24-26, 1999.

[36] B. Wang, "Detached-eddy Simulation of Flow Non-linearity of Fluid-Structural Interactions Using High Order Schemes and Parallel Computation." Ph.D. Thesis, University of Miami, November 2008.

[37] P. Roe, "Approximate Riemann Solvers, Parameter Vectors, and Difference Schemes," *Journal of Computational Physics*, vol. 43, pp. 357–372, 1981.

[38] B.-Y. Wang and G.-C. Zha, "Comparison of a Low Diffusion E-CUSP and the Roe Scheme for RANS Calculation." AIAA Paper 2008-0596, 46th AIAA Aerospace Sciences Meeting and Exhibit, Jan. 7-10, 2008.

[39] J. R. Edwards, "A Low-Diffusion Flux-Splitting Scheme for Navier-Stokes Calculations." AIAA Paper 95-1703-CP, June, 1995.

[40] J. R. Edwards, "A Low-Diffusion Flux-Splitting Scheme for Navier-Stokes Calculations," *Computer & Fluids*, vol. 6, pp. 635–659, 1997.

[41] A. Jameson, "Time Dependent Calculations Using Multigrid with Applications to Unsteady Flows Past Airfoils and Wings." AIAA Paper 91-1596, 1991.

[42] J. M. Délery, "Experimental investigation of turbulence properties in transonic shock/boundary-layer interaction," *AIAA Journal*, vol. 21, 1983.

[43] J. S. Mohler, "Wind-US Unstructured Flow Solutions for a Transonic Diffuser." NASA/CR-2005-213417, 2005.

[44] G.-C. Zha, "Calculation of Transonic Internal Flows Using a High Resolution Upwind Scheme." Submitted to AIAA 42nd Aerospace Sciences Meeting, Jan. 2004, Reno, NV, Jan. 2004.